Dissertation
submitted to the
Combined Faculties for the Natural Sciences and for Mathematics
of the Ruperto-Carola University of Heidelberg, Germany
for the degree of
Doctor of Natural Science

presented by
Diplom-Physiker Marcus Dyba
born in Lübeck, Germany
Oral examination: Februrary 11th, 2004

STED-4Pi Microscopy

Referees: Priv. Doz. Dr. Stefan W. Hell
Prof. Dr. Josef Bille

Zusammenfassung:

Gesättigte Entvölkerung durch stimulierte Emission (engl.: stimulated emission depletion, STED) durchbricht die Abbesche Auflösungsgrenze in der Fluoreszenz-Mikroskopie. Dabei wird die Fluoreszenz durch einen Abregungs-Laserpuls im fokalen Randbereich verhindert. In dieser Arbeit wird theoretisch und experimentell gezeigt, dass die Kombination mit einer weiteren Technik, der 4Pi-konfokalen Mikroskopie, zu bisher unerreichten Axialauflösungen in der Lichtmikroskopie führt. Zentraler Teil der Arbeit ist der Aufbau eines solchen STED-4Pi Experiments. Simulationen sagen eine Überauflösung von etwa 30 nm voraus, die an dünnen Fluoreszenzschichten verifiziert wird. Dieses Ergebnis gilt als bisher beste Axialauflösung eines Lichtmikroskops. Erste biologische Bilder mit 40-50 nm Auflösung werden an membrangefärbten Bakterien gewonnen. Ein zentrales Problem dieser Technik ist die Fotostabilität der Farbstoffe. An den Bakterien wird exemplarisch gezeigt, dass Verlängerung der Abregepulsdauer zu deutlich höherer Fotostabilität führt. Ein unter STED-Bedingungen stabiler, amino-reaktiver Farbstoff ermöglicht die ersten überaufgelösten Immunofluoreszenz-Aufnahmen an Säugerzellen mittels STED-Technik. Diese haben eine Auflösung von 50 nm entlang der optischen Achse. Abschließend wird gezeigt, dass im STED-4Pi Mikroskop zusätzlich STED-Techniken zur lateralen Auflösungserhöhung einsetzbar sind. Damit wird zukünftig eine simultane Überauflösung von mindestens 100 nm lateral und 50 nm axial möglich werden.

Abstract:

Saturated stimulated emission depletion (STED) has been shown to break Abbe's resolution limit in fluorescence microscopy. This technique suppresses fluorescence at the focal rim by use of a depleting laser pulse. In this thesis, theoretical and experimental examinations show that the combination with another technique, namely 4Pi-confocal microscopy, leads to a yet unreached axial resolution in light microscopy. The central part of this work is the performance of a STED-4Pi experiment. Simulations predict a superresolution of about 30 nm that is confirmed in experiments with ultrathin fluorescent layers. These results are so far considered to have the highest axial resolution for a light microscope. First biological images are recorded with membrane labeled bacteria at 40-50 nm resolution. A major issue is the photostability of the fluorescent dyes. With the bacterial samples, it can be exemplarily demonstrated that longer depletion pulses increase photostability. An amino-reactive dye, that is stable under STED conditions, enabled the first superresolved mammalian immuno-fluorescence images. They reveal a resolution of 50 nm along the optic axis. Finally, a further implementation of an additional STED beam for lateral resolution enhancement is demonstrated. In future, this will enable simultaneous superresolution of at least 100 nm in the lateral and 50 nm in the axial direction.

List of abbreviations

1D	one-dimensional
3D	three-dimensional
4Pi	Optical microscope with axially enhanced resolution achieved by a focused standing wave
AFM	Atomic force microscopy
EM	Electron microscopy
FCS	Fluorescence correlation spectroscopy
FLIM	Fluorescence lifetime imaging
FRET	Fluorescence resonant energy transfer
FWHM	Full Width at Half Maximum
GSD	Ground state depletion
HEK	Human embryonic kidney
I^5M	Optical microscope with axially enhanced resolution by a focused standing wave in wide-field mode
LPC	laser power controller
NA	Numerical aperture of a lens
NIR	Near infrared
OPO	Optical parametric oscillator
OTF	Optical transfer function
PSF	Point spread function
SHG	Second harmonic generation
SNOM	Scanning nearfield optical microscopy
STED	Stimulated emission depletion
STM	Scanning tunneling microscopy
Ti:sapphire	(modelocked) Titannium:sapphire laser
TIR,	
TIR-FM	Total internal reflection (-fluorescence microscopy)
TPM	Two photon microscopy

Contents

1 Introduction **2**

1.1 Roads to the nanoscale . . . 2

1.2 Modern optical farfield microscopy . . . 3

1.3 Stimulated emission depletion microscopy . . . 6

2 STED in a 4Pi-confocal microscope **10**

2.1 Concept and Calculations . . . 10

2.2 Experimental Setup . . . 13

2.3 Experimental verifications . . . 14

2.3.1 Axial responses with 33nm width . . . 14

2.3.2 Separation of identical objects below the diffraction barrier . . . 18

2.4 Optical transfer function . . . 18

3 STED imaging of cell membranes **24**

3.1 Imaging of RH414 labeled *bacillus megaterium* . . . 24

3.2 Photostability studies under STED conditions . . . 25

4 Immuno-fluorescence STED imaging **34**

4.1 Improvement of the STED-4Pi setup . . . 34

4.2 STED dye MR-121SE for immuno-labeling . . . 36

4.3 Mammalian microtubules at 50 nm axial resolution . . . 38

4.4 Lateral superresolution in immuno-fluorescence imaging . . . 41

5 Conclusion **44**

Chapter 1

Introduction

1.1 Roads to the nanoscale

It is part of the human nature to observe the environment to gain knowledge about the world. “Looking closer” at objects and subjects is therefore one of the major tasks of science. While “looking” in this literary sense can of course have a wide range of meanings and involves very different technologies, optical imaging is for sure one of the essentials. Incipient with telescopes for the large scale, it extends to optical microscopes which were the first breakthrough-technology for modern biology [33]. Still today, optical microscopy is one of the key technologies in cell biology since looking inside the interior of a functioning cell can only be performed by light. Unfortunately, the wave-nature of light does not allow a representation of details smaller than $0.61\lambda/NA$ [64], where λ is the vacuum wavelength of light and NA the numerical aperture of the imaging system (e.g. the lens). This fundamental law, referred to as the *diffraction limit*, was discovered in 1873 by Ernst Abbe [1]. Till this day, it still holds true if the task is to describe the focusing process of light. From the knowledge of our days it has to be revised to some extent if it is concerned with the imaging process under specialized conditions [24]. However, for an ordinary optical microscope, it limits the resolution to about 200 nm in the lateral and 500 nm in the axial direction (along the optic axis). Therefore, during the last century, a lot of subtle developments took place to obtain more detailed images.

One attempt is to reduce the wavelength λ since the NA can reach a value of 1.4-1.6 at the most[1]. This is realized in x-ray microscopy where wavelengths of 2-4 nm are used. Because of lack of high refractive index materials, (diffraction based) Fresnel lenses need to be used for x-ray optics and a resolution of 30 nm has been reported [52]. X-ray radiation is of course not compatible with live cells and therefore only applicable in-vitro. Additionally, the limited number of high intensity x-ray sources at the moment excludes its wide spread use.

Another approach is the use of matter waves, since its de Broglie wavelength is as short as about 10^{-3} nm (for a typical electron microscope) . High energy electron beams are used in electron microscopy (EM) [65] and a resolution of 0.1 nm can be obtained in biological samples. Since this technique has a resolution better than the size of a typical protein (5 nm), it is widely used in cell biology. EM-sample preparation involves cutting the sample into thin slices and, in most cases, marking them with contrast enhancing materials such as gold. Snapshot-like images of cellular structures can be recorded by rapidly freezing the sample to

---

[1] The numerical aperture is limited technically and by the availability of optical materials with high refractive indices.

low temperatures during a timescale of some milliseconds, while the imaging process itself lasts longer. Focusing is realized through electromagnetic forces supplied to the electrons.

Scanning probe microscopes utilize a tip or solid sensor that is scanned above the surface of the object under investigation. The tip-surface interaction gives the contrast parameter for the obtained images. In atomic force microscopy (AFM), the electromagnetic interaction between one atom (or a cluster) at the tip-apex and the surface is used [4]. Another approach is to measure the tunneling currents from the tip to the surface (scanning tunneling microscopy, STM) [5, 6]. Scanning probe microscopes reach atomic resolution, but they are inherently surface bound.

The scanning nearfield optical microscope (SNOM) [71, 61, 49] is an optical microscope that does not use focused light and is therefore not diffraction limited. The trick is to use a nanoscaled tip with a light emitting aperture much smaller than λ. Whereas the escaping light propagates divergently away from this aperture according to the diffraction theory, in the so called nearfield region, the area of illumination is defined by the dimension of the aperture itself, not by the wavelength. While the tip is scanned over the surface, the illuminated area has a dimension of 50-100 nm. Pulled optical fibers coated with metal are commonly used as tips. In this case, the penetration depth of light (approx. 10 nm in metals) limits the achievable resolution to about 20 nm in theory which, to my knowledge, has not been met in practice, as yet. One of the main problems is the light throughput through the fiber. Besides, the distance to the surface has to be held constant. To control this, mechanical shear rate *(tapping mode)*, an AFM or STM has to be used. Therefore, the optical contrast may just represent the force or tunneling contrast, which causes the risk of image artifacts [21]. The implementation of different tip systems, e.g. a single molecule acting as a nano-antenna, may enable nearfield resolution in the nanometer range [82, 67, 53]. Total internal reflection (TIR) microscopy also uses nearfield excitation to improve the axial resolution down to the penetration depth of light. Therefore, the evanescent wave at total reflection is used for illumination [70, 2, 74]. However, both nearfield versions are as well surface bound.

In conclusion, among all the state-of-the-art technologies, the optical farfield microscope, based on focused light, is the only way to image the interior of live cells. Because of that reason, the optical microscope, despite its comparatively low resolution, remained the workhorse in cell biology and medical science. Improvements in imaging speed and spatial resolution are of great interest and took a lot of effort during the last decades. A brief overview of important developments is given in the next section.

1.2 Modern optical farfield microscopy

Starting from the end of the 19^{th} century, the field of optical microscopy was almost stagnating for nearly 100 years, while the number of applications dramatically increased. The reason is that after the development of Abbe's diffraction theory in Jena, the Carl Zeiss company already in those days was able to produce (apochromatic) microscope objectives with diffraction limited resolution of $\approx 1/4\ \mu$m. While the focusing optics was optimized in the meantime, the discovery of the laser initiated a modern renaissance of optical microscopy.

The laser scanning microscope [81] utilizes focused laser light to illuminate the specimen. If the focal spot is scanned through the object, the recorded signal (e.g. reflected, transmitted, scattered or fluorescence light) point by point reveals the image of the sample. This concept became only possible after the availability of lasers, since no intense point light source existed before that could have been focused to a diffraction limited spot. The focal light distribution is called the *point spread function* (PSF). The PSF can be interpreted as the signal response, i.e. the image, of a point object. Thus, its meaning is very essential since the spatial extent of the PSF determines the smallest dimension that can be resolved in the image. The smaller the PSF, the finer the details that can be reproduced, if scanned through the focus; a huge PSF would blur tiny structures. For increasing the resolving power, the goal is to produce a PSF as small as possible. As mentioned, an easy but restricted way is to shift λ to shorter values, besides using objectives with a maximal numerical aperture, leading to $\approx$ 180 nm lateral resolution. Further, the often innovative advances in designing small PSF are referred to as *point spread function engineering.*

One of the earliest innovations in scanning microscopy was the confocal microscope [54]. Useful versions became possible by the use of lasers and digital data recording in the late 1980's [80, 60]. In a confocal arrangement, the object is illuminated by the focused spot produced by a point source of light. In fluorescence microscopy, it is referred to as excitation PSF, h_{exc}. The detection signal is imaged again by the objective onto a point detector, i.e. a spatial filter smaller than the Airy disk of the imaged detection light. Light coming from regions outside the proper focal volume, i.e. from the cones of the focused excitation light above or beneath the focal plane, will be defocused at the point detector and therefore will not contribute to the signal. By this discrimination the of out-of-focus light, the confocal microscope for the first time enabled a real 3D resolution. The detection process can be described by a probability distribution at the focal area for a signal photon to be detected by the point detector. This distribution is depicted by the detection PSF, h_{det}. In the same way, an excitation PSF can be seen as the probability distribution for the interaction of the excitation light with the specimen. The overall probability for detecting a photon therefore is given by the confocal PSF

$$h_{conf}(\vec{r}) = h_{exc}(\vec{r}) h_{det}(\vec{r}) \simeq h_{exc}(\vec{r})^2. \tag{1.1}$$

The identity of (1.1) is valid, if excitation and detection wavelength are the same, and if the detector has a vanishing diameter. The multiplication of both PSF's leads to a quadratic suppression of outer focus light, which enables the real 3D performance with an axial resolution of $\approx \lambda$. Also the lateral resolution is improved by the detection process compared to a standard light microscope. Today, the confocal microscope can be seen as the standard device for high-end biological imaging and spectroscopic applications down to single molecule sensitivity. Therefore, the developments in this thesis are compared to a confocal setup.

Also other approaches were successful, like two photon fluorescence microscopy. Here, a nonlinear absorption process is utilized, that was first predicted by Maria Göppert-Mayer in the 1930's [14]. Two photon absorption is a quantum-electronical process of the concomitant absorption of two photons with energy $h\nu$ that provide a single excitation energy of $2h\nu$. For pronounced two photon absorption, high electromagnetic field energies are needed, which made the experimental realization not possible until the availability of ultrashort laser pulse sources [7]. The absorption is proportional to the square of the light intensity and that limits the fluorescence excitation to the high intense focal area of a microscope. Similar to the confocal principle, this yields a quadratic dependence of the (effective) PSF on the light field, i.e. $h_{2photon} \propto h_{exc}^2$. Two photon microscopy (TPM) enables optical 3D sectioning in the same way as a confocal microscope even without a detection pinhole. This makes TPM useful for highly scattering samples as brain slices or tissue. The fluorescence is known to be excited only in the confined volume of the focus and can be collected without further spatial restrictions.

Also important, the doubled wavelength compared to single photon absorption enables deep focusing in highly scattering media. This made TPM an important tool in neuroscience and tissue research that enables nearly confocal resolution. However, increased photobleaching and expensive laser sources prevent a broad application in cell biology.

Further novel techniques take advantage from interference of two counterpropagating fields focused through two opposing lenses. These concepts are a prime example of PSF engineering, since the PSF has inference maxima more compact in the axial direction by a factor of $\approx 4-5$. The doubled effective numerical aperture yields 90-140 nm axial resolution. 4Pi microscopy [23, 25] works in a confocal setup with either one or two photon excitation , I^5M [20, 18] is a widefield version working with illumination from a common lamp and standing wave microscopy [47, 3]is a low numerical aperture version useful for axial distance measurements only.

As in the confocal concept, the lateral resolution can also be improved by a factor of about 2 through structured illumination patterns created in the entrance pupil of the objective [19]. Final deconvolution is needed to reveal the image. This technique uses widefield microscopes and can for example be combined with a I^5M setup. For point scanning microscopes, an analogous approach utilizes phase masks in the entrance pupil.

An early and intriguing concept of PSF engineering based on phase modulation of the incident wavefront should be mentioned here too. Toraldo di Francia proposed in 1952 that the focal distribution can be arbitrarily adjusted at n points if the phase of light is skillfully shifted in n rotationally symmetric ring zones of the aperture [75]. For n$\rightarrow \infty$, this enables central peaks of light, to be as sharp as desired. In this theory, the Abbe limit can be broken by subtle phase modulation of the incident wave. This becomes possible since the concept is related to the intensity distribution of light, while the contributing field amplitudes of each ring zone itself are all in the Abbe range. **For definition, in this thesis, the resolution is called *sub-diffraction* sized if the corresponding optical transfer function contains frequencies above the Abbe limit.** In Toraldo's concept, diffraction inherently enforces that light is diverted away from the focal point. The smaller the central peak is designed, the larger will be the amount of deviated light. In other words, in the Fourier depiction, the optical bandwidth can be exeeded without limit, but the amplitudes of really high frequencies will be strongly attenuated. For a realistic signal-to-noise ratio, the attainable resolution gain ought to be less than an order of magnitude, always requiring image deconvolution. To the best of my knowledge, not more than only PSF-measurements were so far realized.

Important progress in the field of studying molecular processes at the nanoscale was achieved by spectroscopic approaches, accepting the limited resolution of a light microscope. A review of cell biological applications of this fast developing field is given for example in [50]. Fluorescence correlation spectroscopy (FCS) allows the investigation of diffusion, molecular dynamics and chemical reaction in solution and also in live cells. Fluorescence lifetime imaging (FLIM) uses the lifetime of the excited state to create an image contrast that is sensitive to the chemical environment of fluorophores, unfortunately with low dynamics. Fluorescence energy transfer (FRET) became a prominent way to analyze colocalisation and chemical binding of compounds. FRET is a process that transfers energy from an excited donor molecule to an acceptor due to a nearfield dipole-dipole interaction. FRET is efficient only for distances smaller the Förster radius of typical some nanometers and scales with r^{-6}, if r is the dipole distance. Thus, (red shifted) fluorescence of the acceptor can only be observed, if a donor is present inside the Förster radius. An acceptor signal therefore is an indicator for chemical binding or colocalisation. In conjunction with immunolabeling techniques and genetic coded

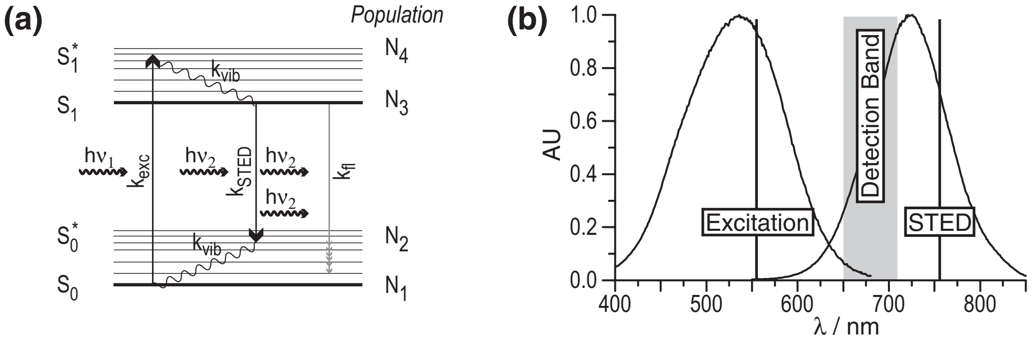

Figure 1.1: **Spectroscopic STED diagrams.** (a) 4-Level Jablonski diagram of a dye molecule that sketches one STED cycle. k_{exc} is the excitation rate from the ground state S_0 to the vibronical excited state S_1^*, k_{fl} and k_{STED} are the free and induced relaxation rates to the vibrational excited state S_0^*. (b) Excitation and emission spectra of a typical far-red emitting STED dye (RH414). Also marked are the spectral positions of the laser lines and the fluorescence detection range. STED is normally applied at the red edge of the Stokes shifted fluorescence spectrum to prevent residual reexcitation.

fluorescent proteins as GFP, YFP and DsRED [76, 51], this is a innovative tool to study molecular proximities without having molecular resolution [62, 44].

However, a resolving power in the nanometer range with a focusing light microscope would be an ultimate tool for any cell biologist, since it still will be the only way to study the nanostructure of cell organelles. A couple of years ago, this was believed to be impossible. During the past years, this goal seems to become achievable by the invention of saturation based microscopy, where one of the most promising techniques is stimulated emission depletion (STED).

1.3 Saturated stimulated emission depletion (STED) microscopy

Important improvements in light microscopes have been realized. But all of them – except the nearfield based SNOM and TIR-FM – still are restricted by the wavelength. Progresses in the field of high resolution optical microscopy became possible through the availability of laser light. An innovative idea of really breaking the diffraction resolution limit in fluorescence microscopy [30] is related to lasers in a direct manner: The concept of stimulated emission depletion does not only use laser sources for its implementation, but very essentially benefits from the underlying principle of any laser, stimulated emission, that was first predicted in 1917 by A. Einstein [12].

The basic idea is to reduce the focal extent of a fluorescence microscope by cancelling out fluorescence emission of excited molecules at the edges of the excitation PSF. The prohibition of fluorescence is achieved by a competing process that is much more effective: stimulated emission. In order to realize that, fluorescence molecules are excited by ultrashort laser pulses to the vibronic state S_1^* within the diffraction limited focus of a common objective lens (see Fig. 1.1(a)). After fast thermal relaxation to the vibrational ground state S_1, a subsequent red-shifted laser pulse (STED pulse) couples excited molecules back to a vibrational excited ground state S_0^*. The excitation energy is carried away by a (stimulated) photon, that is indistinguishable from the (stimulating) photon of the STED pulse. As already predicted by Einstein, the light induced coupling of $S_1 \leftrightarrow S_0^*$ not only opens up stimulated emission $S_1 \rightarrow S_0^*$, but also absorption $S_1 \leftarrow S_0^*$ with the same probability. Similar to the situation in a laser medium, the population of both levels could only equilibrate. This would mean only half a suppression of fluorescence. Fortunately, the thermal relaxation $S_0^* \rightarrow S_0$ with $k_{vib} \approx 10^{11} - 10^{13}$ sec^{-1} immediately empties the population of S_0^* and prevents further re-absorption steps. Thus, for $t \gg k_{vib}^{-1}$ a complete transfer of the S_1-population to S_0 can be achieved. Therefore, the STED-pulse duration τ has to be $\gg k_{vib}^{-1}$. On the other hand, the transfer has to happen much faster than the fluorescence emission due to the spontaneous decay with the lifetime $k_{fl}^{-1} \approx 10^{-9}$ sec. This gives the important condition on the length of the STED pulse

$$k_{vib}^{-1} \ll \tau \ll k_{fl}^{-1}, \tag{1.2}$$

that determines the STED-pulses to be in the range of some 10-100 ps. For a complete depletion of the excited molecules, the transition probability for stimulated emission, σh_{STED}, has to be $\gg 1$. σ is the cross-section for stimulated emission. h_{STED} is the pulse photon density, meaning the number of photons crossing the unit area per pulse.

If the STED pulse fulfills these conditions and does not excite the molecules from the ground state itself, it hinders the emission of fluorescence in a non-invasive way. The spatial distribution of the STED focus $h_{STED}(\vec{r})$ (referred to as STED-PSF) is chosen such that no intensity is focused into the focal point, but in its direct proximity. Hence, molecules at the rim of the excitation spot will remain “inactive” and fluorescence originates only from the center of the excitation focus. This has the same effect as squeezing the excitation point spread function to smaller extents, which is not possible due to the wave-nature of light.

For a detailed mathematical and spectroscopic description of the STED effect and its implementation in microscopy see e.g. [24, 37]. Here, important aspects and formulas related to its capability of breaking the diffraction resolution limit are shortly discussed. The spectroscopic behavior of an organic molecule can be described by a four-level energy scheme (Jablonski diagram), as shown in Fig. 1.1(a) [45]. Its dynamic behavior in a STED experiment is described by a system of four partial differential equations for each energy level

$$\frac{\partial}{\partial t}N_1(t) = k_{exc}(t)[N_4(t) - N_1(t)] + k_{vib}N_2(t) \tag{1.3}$$

$$\frac{\partial}{\partial t}N_2(t) = k_{fl}N_3(t) - k_{STED}(t)[N_2(t) - N_3(t)] - k_{vib}N_2(t) \tag{1.4}$$

$$\frac{\partial}{\partial t}N_3(t) = -k_{fl}N_3(t) + k_{STED}(t)[N_2(t) - N_3(t)] + k_{vib}N_4(t) \tag{1.5}$$

$$\frac{\partial}{\partial t}N_4(t) = -k_{exc}(t)[N_4(t) - N_1(t)] - k_{vib}N_4(t), \tag{1.6}$$

where $N_1, ..N_4$ are the population numbers of the four energy levels, $k_{exc}(t)$ the excitation rate, k_{fl}, k_{vib} the electronical and vibrational relaxation rates of the molecule, and $k_{STED}(t)$

the induced transfer rate by the STED pulse. It has been assumed that the vibrational rate k_{vib} for the S_0 and S_1 manifold are equal. $k_{exc}(t)$ and $k_{STED}(t)$ are time dependent due to their pulsed action. It is $k_{STED} = \frac{\sigma h_{STED}}{\tau}$ during STED pulse action, if rectangular shaped pulses are assumed for simplicity.

The effect of fluorescence inhibition can be clarified under the simplifying condition that $k_{vib} = \infty$.[2] Thus, during a well defined excitation pulse length, N_0 molecules are transferred to S_1 by the excitation pulse ($N_4(t \geq 0) = 0$; STED begins at t=0). Besides, molecules fall directly to S_0 during STED ($N_2(t) = 0$). Then, the solution of (1.5) yields a population of S_1 directly after the STED pulse duration τ, that is given by

$$N_3(\tau) = N_0 \exp(-[k_{fl} + k_{STED}]\tau) = N_0 \exp(-k_{fl}\tau)\exp(-\sigma h_{STED}).$$

Compared to the situation without stimulated emission ($h_{STED} = 0$), the amount of exited molecules (N_3) – and therefore the fluorescence signal – is reduced by

$$\eta(h_{STED}) = \exp(-\sigma h_{STED}). \tag{1.7}$$

η is called the STED suppression coefficient, since it describes the amount of fluorescence inhibition. $\eta(h_{STED})$ is a function that is accessible by experiments and can vary under real conditions. However, also for real molecules, (1.7) is a good approximation if the vibrational relaxation is short compared to the STED pulse duration, and if the STED pulse does not prevent fluorescence by further processes, e.g. photobleaching. For numerical simulations of $\eta(h_{STED})$ see [37]. Experimental depletion curves are published in [38, 40, 78, 8, 9].

The most important aspect of (1.7) is the strongly nonlinear dependency of the remaining fluorescence on the STED intensity, which is caused by a saturation behavior of STED. Any arbitrary small amount of leftover fluorescence $\delta\eta \ll 1$ can be achieved by a finite value of h_{STED}. Any further increase has only small consequences on the signal suppression, i.e. STED is saturated. Indeed, Fig. 2.1(d) demonstrates that pronounced saturation curves can be experimentally realized. The actual breaking of the diffraction limit stems from this saturation-nonlinearity, since the STED-PSF $h_{STED}(\vec{r})$ itself still is diffraction limited at its best performance. The final distribution of excited molecules, i.e. the effective point spread function $h_{eff}(\vec{r})$ of the confocal STED microscope is given by the confocal PSF multiplied with the local STED suppression coefficient

$$h_{eff}(\vec{r}) = h_{exc}h_{det}\eta(h_{STED}) \simeq h_{exc}h_{det}\exp(-\sigma h_{STED}). \tag{1.8}$$

$h_{STED}(\vec{r})$ importantly has to support low intensity in the focal point to ensure $\eta(h_{STED}(\vec{0})) \approx 1$. This ensures that fluorescence will be unaffected in the central area. In the surrounding, focused STED intensity suppresses fluorescence. For a certain, finite intensity nearly complete suppression ($\eta \ll 1$) will be reached at the intensity peaks $max(h_{STED}(\vec{r}))$. Further increase of h_{STED} will enlarge the region of full suppression, until a very small volume of exited molecules remains only in the center. Indeed, theoretically this volume can be reduced to molecular scale, if $max(h_{STED})$ is increased to infinity and $\eta = 1$ is ensured at the focal point. Thus, the Abbe limit, as concerned to the smallest extent of focused light, does not at all

---

[2] This is a good approximation, if $\tau \gg k_{vib}^{-1}$ is fulfilled. Only slight deviations would occur under consideration of k_{vib}.

limit the resolution of a STED microscope. Limitations are given in practice by the maximal power that can be applied to the dye molecules under photostable conditions and by residual intensity at $\vec{r} = 0$ due to optical imperfections or scattering.

Also other microscopes that allow sub-diffraction resolution rely on a nonlinear relationship between the intensity of light and a signal related parameter, e.g. the cross-section for absorption (multi-photon microscopy) or stimulated emission (STED). So far, the PSF of a two-photon microscope has to be called sub-diffraction sized, since its excitation volume is shrunk due to the quadratic dependency of excitation on the field energy.

However, there is a major difference to the STED nonlinearity based on saturation. The quadratic nonlinearity in two-photon and confocal microscopy (through nonlinear absorption and multiplication with a detection PSF) gains only resolution enhancement of a constant factor, that is in the order of 1, whereas any saturation based nonlinearity can gain arbitrary resolution. Indeed, also other types of saturation effects could be used, as ground-state depletion (GSD) [28] or saturated pattern excitation microscopy [22]. The theory for these techniques is analogous to STED, if the specific nonlinearity is implemented instead of η. In practice, ground-state depletion is not expected to be very photostable, since it involves triplet states. Unfortunately, saturated excitation automatically entails the need of further image processing, since it initially enlarges the PSF and creates steep edges near the minima. Image information then has to be extracted in the frequency domain. So far the first realization of saturation microscopy was achieved by STED [41, 38].

In this thesis, the first realization of a STED microscope is presented, whose STED-PSF is created in 4Pi-mode. This synergistic combination of STED- and 4Pi microscopy was predicted to be very efficient due to the narrow intensity distribution that is produced by the focused standing wave. Indeed, a unique resolution in the range of tens of nanometers could be verified.

Chapter 2

STED in a 4Pi-confocal microscope

STED is a process where saturated depletion of fluorescence defines the final focal extent rather than the intensity distribution of the focused light. Therefore, the most important requirements are stable fluorophores and matched physical parameters of the stimulating light to achieve a highly efficient depletion of the excited state. Furthermore, an almost complete vanishing of STED light intensity in the focal point is essential to maintain most molecules excited under strong saturation conditions. However, the final resolution is determined by both the STED saturation and the distribution of stimulating light, $h_{STED}(\vec{r})$.

All optical requirements concerning a narrow central minimum and good control of its intensity through interference are fulfilled in a 4Pi microscope, if used to form the STED-PSF [8, 69, 31]. In a 4Pi-confocal microscope, the focus is produced by coherently focusing light through two opposing lenses. The central peak of the interference pattern is 4-5 fold smaller in the axial direction compared to a standard confocal microscope [23]. While this technique itself produces images with ≈100 nm axial resolution, here the interference based PSF is used for stimulated emission. For this purpose, the relative phase of the two counter-propagating waves in the focal point $\vec{r} = \vec{0}$ is set to π, leading to destructive interference. Due to the doubled effective numerical aperture of a 4Pi microscope the central minimum with an axial FWHM of $\approx \frac{\lambda}{4n}$ is much smaller than that of single lens techniques [38]. In fact, resolution enhancement by 4Pi microscopy and STED are based on completely different processes that add up. In this chapter, the implementation of STED in a 4Pi microscope will be discussed and experimental verification for axial resolutions down to 33 nm will be presented. Results of this chapter are partly published in [8].

2.1 Concept and Calculations

The implementation of STED can be realized by coupling two pulsed and synchronized laser beams (for excitation and STED) into a 4Pi microscope. This is done in a way that the excitation pulses pass into the focus through one of the two objective lenses only. After a delay in the picosecond range, the STED pulses are propagating in opposite directions through both lenses and build up a standing wave with destructive interference in the focal point, shortly called *destructive 4Pi-PSF*. The remaining fluorescence is collected in an epifluorescence mode by the excitation lens and confocally detected by a point detector.

Following the focusing theory by Richards and Wolf for high numerical apertures [66], the focal intensity distribution of a (aplanatic) 4Pi-PSF is given by

$$h_{STED}(\vec{r}) = \frac{n^2\lambda\varepsilon_0\tau}{2h}|\vec{E}_1(\vec{r})+\vec{E}_2(\vec{r})|^2 \tag{2.1}$$

with

$$\vec{E}_1(r,z,\phi) = \frac{-iE_0nf}{\lambda}\int_0^{\alpha}\int_0^{2\pi}\sqrt{\cos\vartheta}\sin\vartheta\exp\{i[\Psi(\vartheta)+k(s-f)]\}\times\begin{pmatrix}\cos^2(\phi'-\phi)\cos(\vartheta)+\sin^2(\phi'-\phi)\\ \sin(\phi'-\phi)\cos(\phi'-\phi)[\cos\vartheta-1]\\ -\cos(\phi'-\phi)\sin\vartheta\end{pmatrix}d\phi' d\vartheta$$

and

$$\vec{E}_2(r,z,\phi) = \begin{pmatrix}1&0&0\\0&-1&0\\0&0&-1\end{pmatrix}\vec{E}_1(r,-z,-\phi)\exp(\Delta\Psi),$$

where h_{STED} denotes the PSF in photons (per STED pulse) per area and $\vec{E}_{1,2}$ the electric field amplitude in cylindrical coordinates for each objective, respectively. E_0 is the pulse-averaged amplitude at the lens entrance pupil, c the vacuum speed of light, ε_0 the permittivity of free space, f is the focal length, s the path from the point (f,ϑ,ϕ') on the converging wave front to (r,z,ϕ), and $k=\frac{2\pi n}{\lambda}$ the wave number in a medium with refractive index n. $\Delta\Psi$ is the relative phase shift of the two (identical) wavefronts of both lenses. $\Delta\Psi$ is zero for a constructive and π for a destructive 4Pi-PSF, respectively. The aberration function $\Psi(\vartheta)$ describes the phase deviation of the converging wave front from a spherical one. For unaberrated systems, it is $\Psi(\vartheta)\equiv 0$. The excitation and detection PSF h_{exc}, h_{det} can easily be calculated by the use of Formula (2.1), setting $\Psi(\vartheta)=0$, $\vec{E}_2=\vec{0}$ and using the correspondent wavelength λ_{exc}, λ_{det}.

Since a destructive 4Pi-PSF exhibits a central minimum and neighbored maxima with a distance of $\approx \lambda/2n$, it is highly appropriate for STED microscopy. This is especially true, because of the smaller distance of axial maxima compared to light distributions used so far for axial resolution enhancement [38, 39]. Additionally, a sensitive control of the central minimum can be realized by adjusting the intensities and polarizations of the two beams in each interferometer path.

However, the 4Pi-PSF will exhibit higher order minima that, if used for the depletion process, will remain fluorescent at the location of these minima. Thus, the effective STED-4Pi-PSF would have fluorescence sidelobes similar to the situation in a standard 4Pi microscope. To eliminate these sidelobes, one can introduce a specially designed aberration function $\Psi(\vartheta)$ prior to the beamsplitter of the 4Pi interferometer. This leads to an identical wavefront shape in both interferometer paths. If adjusted to destructive phase $\Delta\Psi=\pi$ in the focal plane, any part of the converging wavefront still will cancel out with the corresponding part of the opposite wavefront. Thus, the PSF will conserve the central vanishing point of intensity due to the symmetry of the 4Pi microscope. In general, this holds no longer true for offset points of the focus (i.e. for the former higher order minima), because the propagation behavior of both beams is changed. In principle, any $\Psi(\vartheta)$ will retain the zero intensity in the focal plane [26]. For the goal of efficient depletion at the axial rim of the spot, at least the minima next

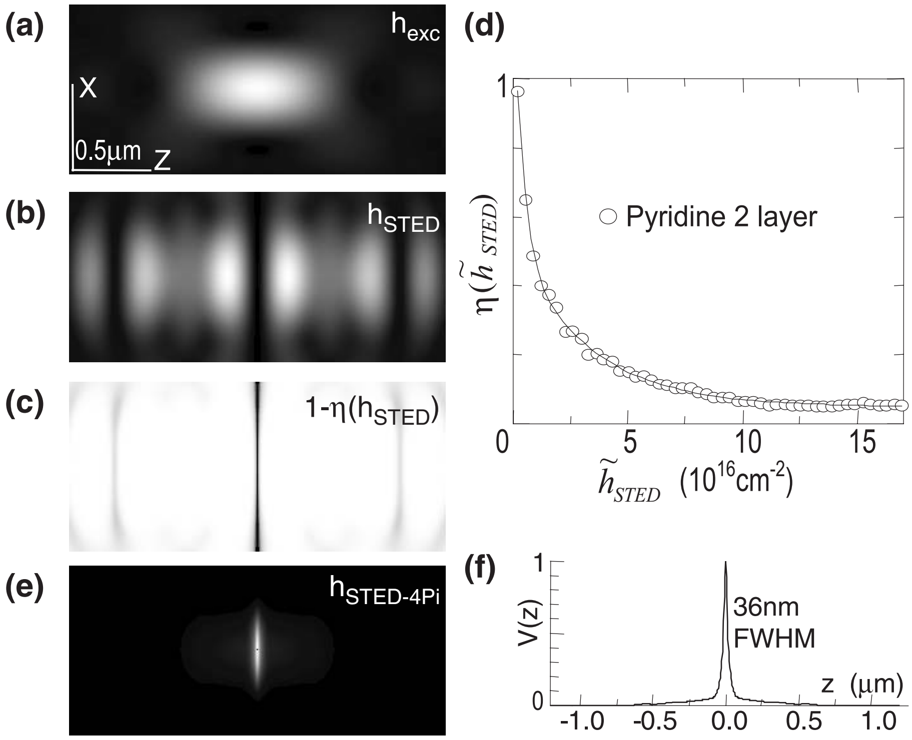

Figure 2.1: **Calculated point spread functions of the STED-4Pi microscope.** (a) Excitation PSF and (b) STED-PSF with destructive 4Pi-interference and an artificial aberration function $\Psi(\vartheta)$, as described in the text. (c) depicts the local depletion $1-\eta(h_{STED})$ under saturation condition with $max(h_{STED})=4\times10^{17}$ cm^{-2}. The underlaying experimental depletion curve is shown in (d), where $\tilde{h}_{STED}$ is the spatialy averaged photon densitiy $ave_{\vec{r}}(h_{STED}(\vec{r}))$. Curve (d) was measured using a standard STED-PSF of kind (a) that was covering h_{exc}. (e) shows the resulting effective PSF and (f) the axial response.

to the central one should be eliminated. Because of the simplicity of manufacturing, a two zone phase filter

$$\Psi(\vartheta) = m\pi\Theta(\vartheta - P\alpha) \tag{2.2}$$

was chosen, where $0 \leq \vartheta \leq \alpha$ denotes the semi-aperture angle and $\Theta()$ is the Heaviside step function. This phase aberration e.g. can be produced by a circular phase delaying coating placed in the inner part of the entrance aperture ($\vartheta \leq P\alpha$). Thus, a plane incident wave will be changed to an inner and outer part, both with a plane wave front, but delayed by $m\pi$.

Calculated point spread functions of the STED-4Pi microscope are shown in Fig. 2.1. Part (a) depicts the excitation spot $h_{exc}(r, z, 0)$, while Fig. 2.1(b) shows $h_{STED}(r, z, 0)$ for $m = 0.4$ and $P = 0.37$ as chosen for all oil immersion objective experiments in this work. For the unaberrated case, all minima along the optical axis have vanishing intensity. In the aberrated case, first and second order minima show finite intensities. Especially, a significant amount of light is distributed at the location of the first order minima.

This light distribution still is diffraction limited with respect to the full numerical aperture of the 4Pi microscope. Bypassing the diffraction limit is achieved by using $h_{STED}(\vec{r})$ under saturated depletion conditions. The effect of saturation can be seen in Fig. 2.1(c) that

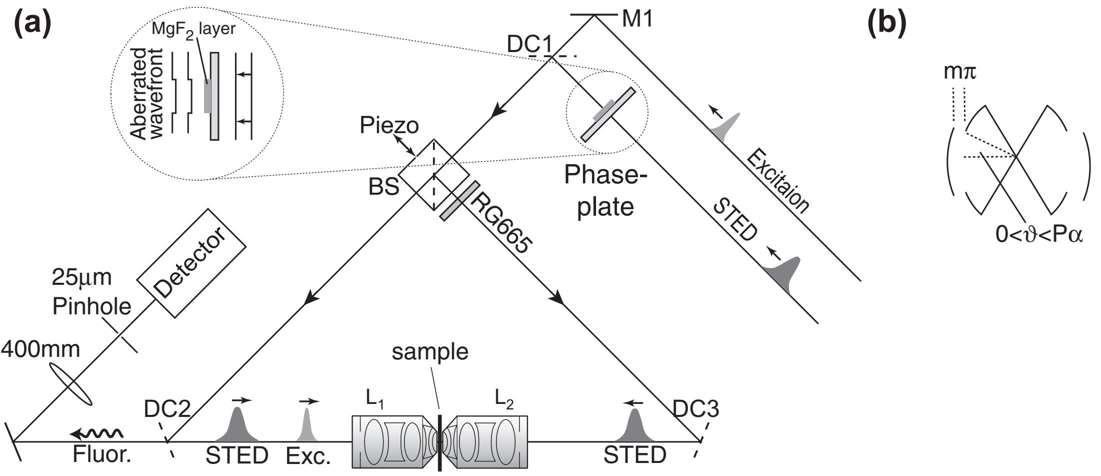

Figure 2.2: **STED-4Pi Setup.** (a) is a schematic sketch of the STED-4Pi microscope as used for the experiments in this chapter. (b) explains how the converging spherical wavefronts of the depletion beam is changed by the two-zone phaseplate.

represents $1 - \eta(h_{STED})$ (see Formula (1.7)). The underlying $\eta(h_{STED})$ as shown in Fig. 2.1(d) was measured at a thin layer of Pyridine 2 molecules adsorbed at the surface of a coverslip. The absolute value of $max(h_{STED}) = 4 \times 10^{17}$ cm^{-2} chosen for calculating Fig. 2.1(c) is in agreement with typical experimental conditions[1]. In the white areas, molecules excited by the spot of Fig. 2.1(a) are efficiently depleted to the ground state. The resulting $h_{eff}(\vec{r})$ presented in Fig. 2.1(d) is calculated according to Formula 1.8. Fig. 2.1(e) shows the axial response $V(z)$, defined by

$$V(z) = \int_0^{2\pi} \int_0^{\infty} h_{eff}(r, z, \phi) r \, dr d\phi. \tag{2.3}$$

The meaning of $V(z)$ is the signal of an infinitely thin fluorescent layer (lying in the (r, ϕ)-plane) scanned along the optical axis z and therefore a good measure to compare with latter experiments. $V(z)$ reveals an axial FWHM of 36 nm. This is a factor 15 smaller than the excitation wavelength λ_{exc}=555 nm used for the calculation and therefore far below the diffraction limit.

Under experimental conditions, the dimension of the remaining spot of excited molecules depends strongly on the depletion curve $\eta(h_{STED})$ and the maximal applicable STED intensity $max(h_{STED})$, that is limited by photobleaching and photo destruction of the sample. However, experiments presented in the next sections will prove the accessibility of the predicted resolution of some tens of nanometers.

2.2 Experimental Setup

For experimental realization of the STED-4Pi concept, a setup schematically sketched in Fig. 2.2 was built. Synchronized laser pulses for excitation and STED are coupled into the microscope via the mirror M1 and the dichroic mirror DC1 overlaying both laser beams. The pulses

---

[1] Assuming a cross section for stimulated emission $\sigma = 10^{-16} cm^{-2}$ for Pyridine 2 this is 40 times over saturation threshold ($\eta = 0.5$).

are produced by a femtosecond laser system consisting of a mode-locked Titanium:sapphire laser[2] and a synchronously pumped parametric oscillator[3] operating at f =76 MHz. Both lasers can be tuned together and STED wavelength of 745 and 760 nm were chosen for all experiments in this chapter. The corresponding OPO wavelength is 554nm and 558nm, respectively.

The ≈250 fs excitation pulses are passed through the beamsplitter BS and reflected by the dichroic mirror DC2 into the objective lens L1 creating $h_{exc}(\vec{r})$. A long pass filter RG665 ensures that excitation light is blocked in the right interferometer arm. The 120 fs Ti:sapphire laser pulses (STED pulses) are stretched by a self-constructed grating stretcher with two holographic gratings[4] to a final duration of τ =13 ps for efficient depletion (see chapter 1). At the beamsplitter BS, the STED pulses split into the 4Pi interferometer paths and are coupled by dichroic mirrors DC2 and DC3 into the objective lenses L1 and L2. The lenses are pairs of oil immersion lenses (NA=1.4) or water immersion lenses (NA=1.2) for the different experiments. Destructive phase ($\Delta\Psi = \pi$) of the 4Pi-PSF is adjusted by a piezo actuator acting on BS. For realizing $h_{STED}(\vec{r})$ of Fig. 2.1, a phase delaying mask was placed into the STED beam prior to BS as shown in the inset. For the phase masks, a circular MgF_2-layer coated on a plane glass substrate is used. The phase plate parameters for oil immersion are $m_{oil} = 0.4$, $P_{oil} = 0.37$ and for water immersion $m_{water} = 0.56$, $P_{water} = 0.57$ (see Formula (2.2)), as used for all experiments in this thesis. The modified converging wavefronts, focused by the objective lenses, are shown in part (b). By using cuvettes with a $CuSO_4$-solution in ethylene glycole, acting as absorption elements with adjustable transmission by changing the concentration, it is ensured that in the common focus of L1 and L2 both beams have the same power with a precision of ≈1-3% (not shown in Fig. 2.2). The linear polarization of the STED pulses is parallel to the excitation polarization.

The sample was placed on a piezo driven 3D scanning stage[5] between the objective lenses and image recording was performed by scanning the sample stage. This ensures better control of aberrations, since beam propagation is fixed along the optical axis. After each pulsed excitation and picosecond delayed STED cycle, the fluorescence of the sub-diffraction sized spot of excited molecules is collected through L1 and DC2 and focused by an achromate (f=400 mm) onto a photon counting avalanche photodiode[6] with a 25 μm fiber. The fluorescence of the used dyes in the range of ≈600-700 nm is separated by a bandpass filter 630-710 nm from the laser lines in front of the detector.

2.3 Experimental verifications

2.3.1 Axial responses with 33nm width

As in any STED experiment, the choice of the fluorescent dye and laser pulse parameters have to be chosen carefully. For the Ti:sapphire laser as a STED pulse source, Pyridine 2[7] is still one of the most unresented functioning dyes. Hence, first experiments were carried

---

[2] *Mira 900F* (Coherent Inc., Santa Clara, CA, USA)

[3] *OPO Advanced* (APE GmbH, Berlin, Germany)

[4] *PC 2200 NIR* with 2200 lines / mm (Spectrogon, AB, Täby, Sweden)

[5] *Nanoblock* (Melles Griot GmbH, Bensheim, Germany)

[6] *SPCM-AQR-13-FC* (Perkin Elmer, Wellesley, MA,USA)

[7] *1-Ethyl-4-(4-(p-Dimethylaminophenyl)-1,3-butadienyl)-pyridinium Perchlorate* (Lambda Physik GmbH, Göttingen, Germany)

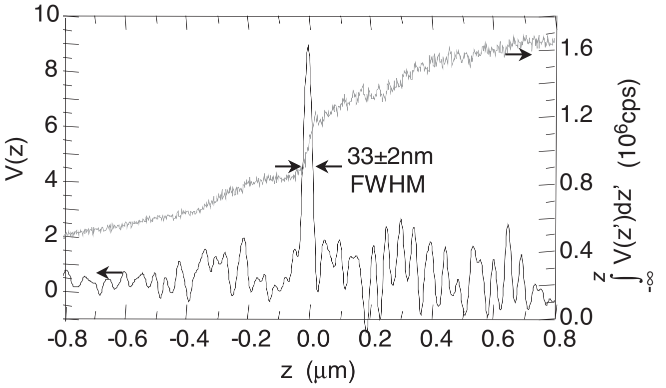

Figure 2.3: **STED-4Pi signal of a fluorescent half space** of Pyridine 2 solved in glycerol (gray line). The derivation reveals the axial response $V(z)$ with a FWHM of 33 nm (black line). The profile was recorded with 7.8 nm axial step size and 1 ms pixel integration time, averaged over 5 scans.

out by placing a solution of Pyridine 2 in glycerol between two coverslips, as needed for every 4Pi compatible sample. When the edge of the solution is scanned along the optical axis z through the focus, the gained signal is described by $\tilde{V}(z) = \int_{-\infty}^{z} V(z')\,dz'$. The derivation $\frac{\partial}{\partial z}\tilde{V}(z) = V(z)$ gives the axial response as defined in Formula (2.3). Data of this experiment are shown in Fig. 2.3. The data were recorded by the use of oil immersion objective lenses (NA 1.4), laser wavelengths of $\lambda_{exc} = 554\,\mathrm{nm}$, $\lambda_{STED} = 760\,\mathrm{nm}$ and a STED power providing $max(h_{STED}) = 7.3 \times 10^{17}\,\mathrm{cm}^{-2}$ in conjunction with an aberration such as (2.2) with $m_{oil} = 0.4$ and $P_{oil} = 0.37$. The gray line shows the raw data of the recorded fluorescent half space. A numerical derivation (black line) was done by the use of a Savitzky-Golay filter that widely conserves the FWHM of the derived peak [63]. At the edge of the fluorescent solution, a sharp peak with a FWHM of 33 nm occurs in good agreement with the predicted axial section in section 2.1. Although a sectioning of about 30 nm can be actually reached, the STED intensity in the experiment was about a factor of two larger than in the simulation. This is due to experimental imperfections of h_{STED}. Especially, even a small amount of residual STED intensity at $\vec{r} = \vec{0}$ leads to a reduction of the peak amplitude. This reduction causes an increased FWHM, that partly can be compensated by increasing the saturation level.

From a pure physical point of view, the curves in Fig. 2.3 from their content are proving the section capability of the STED-4Pi microscope far below the diffraction limit. Since the ultimate breaking of the diffraction limit is caused by the STED light, the focal extent is a factor of 23 smaller than the responsible wavelength. This is not only far below the diffraction limited spot size, but, to my best knowledge, also the smallest spot of exited molecules ever produced with focused light by the use of standard optics.

For a direct measurement of $V(z)$, a layer of fluorophores applicative for STED is needed, which has to be much thinner than the axial resolution. An easily producible sample of an ultra-thin fluorescent layer is available through the obliging property of Pyridine 2 molecules to adsorb on glass surfaces. This effect is reported for very similar compounds of styryl pyridinium dyes on glass surfaces under certain conditions [57, 58]. We observed this effect very pronounced for Pyridine 2 diluted in water. For most other solvents under investigation - e.g. for glycerol as shown in Fig. 2.3 - adsorption could not be seen. We also observed

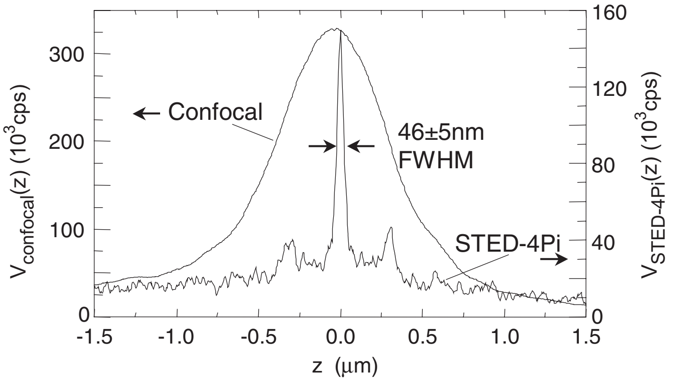

Figure 2.4: **Axial response V(z) measured at an adsorbed ultrathin layer of Pyridine 2** at the coverslip surface. For this measurement, water immersion lenses (NA=1.2) were employed, revealing an axial FWHM of 46 nm. Determination of $V(z)$, as shown here, can be used for linear deconvolution of STED-4Pi images in order to remove the residual sidelobes. The underlying $\eta(h_{STED})$ is that of Fig. 2.1(d). The pixel size is 3.9 nm, and the pixel integration time 1 ms.

a distinct amplification of this effect by illumination with high intensities of the excitation and STED light, especially. Similar effects have been reported also for other compounds [29]. Thus, one can prepare an ultra-thin layer of Pyridine 2 just by placing a ≈10-100 μM aqueous solution between the coverslips[8].

However, the use of water samples causes the need of water immersion objective lenses, which is also a step forward towards biological imaging. At this stage, the sensitivity of STED microscopy to focal aberrations should be mentioned. The saturated depletion of the excited state means a highly nonlinear relationship between the STED intensity and the effect of fluorescence suppression. Thus, even a small amount of light in the central minimum - i.e the areas of remaining fluorescence - will transfer excited molecules back to the ground state in a distinct way. Consequently, aberrations are nonlinearly amplified in the same way. Thus, sample preparation has to be done carefully and the refractive index has to be matched to the immersion medium as well as possible. For water immersion objectives, this also implies a preselection of coverslips in regard to their thickness and a careful adjustment of the correction ring at the objective lens. Importantly, the correction has to be optimized for the STED beam, not for the excitation light, whose action will be undone in the outer regions, anyway. Furthermore, the coverslips have to be adjusted precisely perpendicular to the optic axis. Despite the increased sensitivity of water immersion microscopy there will be no alternative way of applying STED microscopy to live cell imaging.

A measurement of $V_{STED-4Pi}(z)$ on adsorbed Pyridine 2 layers measured with water immersion objectives of numerical aperture $NA = 1.2$[9] is shown in Fig. 2.4. By switching off the STED beam, a confocal response $V_{confocal}(z)$ can easily be recorded afterwards. $V_{STED-4Pi}(z)$, recorded at $max(h_{STED}) = 3.8 \times 10^{17}\,\mathrm{cm}^{-2}$ and $\lambda_{STED} = 745\,\mathrm{nm}$, reveals a FWHM of 46±5 nm. This is narrower than its confocal counterpart by a factor of 17.5±2. At the applied STED power, the peak of the STED-4Pi signal is reduced by 55% compared to

---

[8] The thickness of these layers is estimated to be <10nm because of the number of available molecules in the solution between the coverslips..

[9] *PL APO 63x/1.20 W Corr* (Leica Microsystems AG, Wetzlar, Germany)

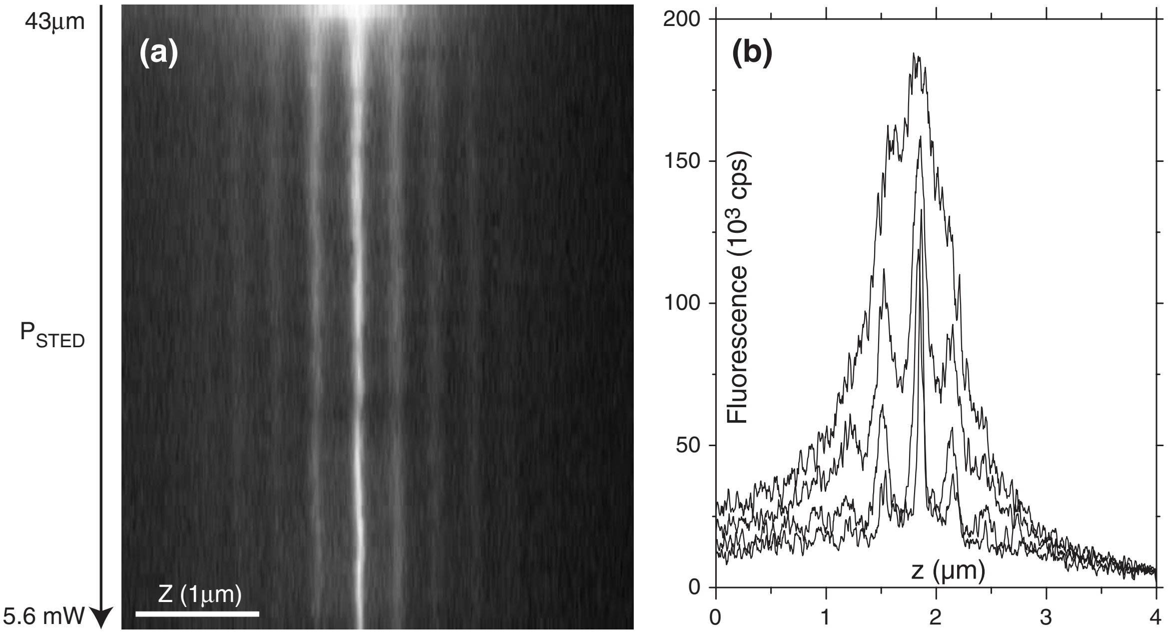

Figure 2.5: $V(z)$ **recorded for increasing STED powers.** The data were recorded at the same conditions as in Fig. 2.4. Additionaly, along the vertical axis the STED power was increased from 43 μW to 5.6 mW, i.e. $max(h_{STED})$ was increased from $8 \times 10^{14}\,\mathrm{cm}^{-2}$ to $3,5 \times 10^{17}\,\mathrm{cm}^{-2}$.

the confocal one. This reduction is caused by residual STED intensity at $\vec{r} = \vec{0}$. One clearly has to separate this signal reduction from the inherent loss of signal while imaging extended fluorescent structures by the reduced detection volume of h_{eff}. In such a case, the inescapable loss of signal is proportional to the reduction of the detection volume needed for the gain of spatial resolution. It just means, that it would make no sense to use a high resolution instrument (supporting high spatial frequencies) for imaging extended structures that need a support for low spatial frequencies, only. In fact, for point structures, the signal loss is only ≈50% in case of Fig. 2.4. This seems to be acceptable in respect of the increased resolution.

Fig. 2.4 also exhibits small side maxima of 18-24% at $z \approx \pm\lambda/2n$. They are originating from incomplete depletion at the side minima of $h_{STED}(\vec{r})$. A linear deconvolution filter can be applied to remove side maxima in STED imaging. Therefore, a recorded $V_{STED-4Pi}(z)$ as shown in Fig. 2.4 can be used to deconvolve images in one dimension (z). As this deconvolution is linear, it does not create new spatial frequencies, which are not present in the raw image, but mainly removes the side maxima. In difference to standard 4Pi microscopy, a complete physical elimination of the side maxima may be done by specially designed $\Psi(\vartheta)$.

The effect of breaking the diffraction limit by saturated STED can nicely be seen by the experiment shown in Fig. 2.5. The image (a) was recorded by scanning the Pyridine 2 labeled coverslip along the axial direction as in Fig. 2.4. Additionally, in the vertical direction, the applied average power of the STED beam was increased line by line. Concomitant lateral translation of the sample ensured scanning on unaffected areas from previous scans[10]. Because of the varying brightness of the sample, the absolute value of the signal can not be compared

---

[10] The brightness of areas depend on the time of STED action. First an increase of signal was observed as reported in the text. Later, photobleaching was observed.

between different lines. For very low STED power of 43 μW, no significant difference to the confocal case can be seen. In the profiles shown in Fig. 2.5(b) only a slight depression of fluorescence at the location of the STED-PSF maxima is present. As expected, complete suppression of fluorescence is achieved at comparatively low power in the maxima regions of $h_{STED}(\vec{r})$. However, final reduction of side maxima and the ultimate squeezing of the central peak happens at higher STED powers, when STED already is highly saturated in the high intensity areas.

2.3.2 Separation of identical objects below the diffraction barrier

The adsorption effect of Pyridine 2 on glass surfaces can also be used to demonstrate the sub-diffraction resolution in its actual sense, i.e. the spatial separation capability of *identical* objects. Identical in this sense means that the objects must not have any physical deviating parameters in terms of their emission of light. Besides, no coherent interaction of light must be present, which is valid for fluorescence anyway.

Since even this strongest formulation of the term *"resolution"* is only determined by $h_{eff}(\vec{r})$, experiments of the previous section are sufficiently proving the sub-diffraction properties of the STED-4Pi microscope. However, an experimental demonstration of the separation capability can be done by preparing a coverslip surface with glass nanoparticles. A sample was produced by disposing silica microspheres of 100 nm diameter out of a water emulsion. The Pyridine 2 solution now adsorbs on the surface of the coverslip as well as on the glass particles.

In Fig. 2.6 axial cross-sections are shown in the confocal mode (a) as well as in STED-4Pi mode (b). Both images were recorded synchronously by switching on and off the STED beam line by line. For each pixel of 3.9×94 nm, the fluorescence was integrated for 2 ms. Residual side maxima are present in (b) as discussed in the previous section. By measuring $V(z)$ in absence of silica particles, the effect of sidelobes can be dealt with a single-step, linear Tikhonov filter [72]. The result is shown in Fig. 2.6(c). One can clearly see the particles laying on the cover slip, while in the confocal reference no structural information about the nanoparticles is present. At their location only increased fluorescence can be observed due to an elevated amount of fluorophores. The inset in part (c) depicts a profile along z through one of the nanoparticles. It reveals a resolved distance of 76 nm between the particle center and the surface with a 42% dip in between. It should be clarified that the deconvolution step does not support this sub-diffraction capacity, as all structural information is obviously already present in (b).

2.4 Optical transfer function

The most precise specification of the optical resolution performance can be given by the concept of *optical transfer functions* (OTF). In this concept one looks on a microscope as a signal processing unit that transfers spatial information from the real object to the image. The structure of the object is described by spatial frequencies $k_{\{x,y,z\}} = 2\pi/\{x,y,z\}$ for the three dimensions of space x, y, z. By a Fourier transformation any structure can be depicted in the frequency space spanned by k_x, k_y, and k_z. Small structures contain high spatial frequencies, while the limiting case of an infinitely extended object just contains a spatial frequency of 0.[11] The microscope itself is described by $h_{eff}(\vec{r})$ in space and by its Fourier transform $\tilde{F}(h_{eff}(\vec{r}))$

---

[11] Mathematically spoken, the Fourier transformation of x=1 is the delta function $\delta(x)$.

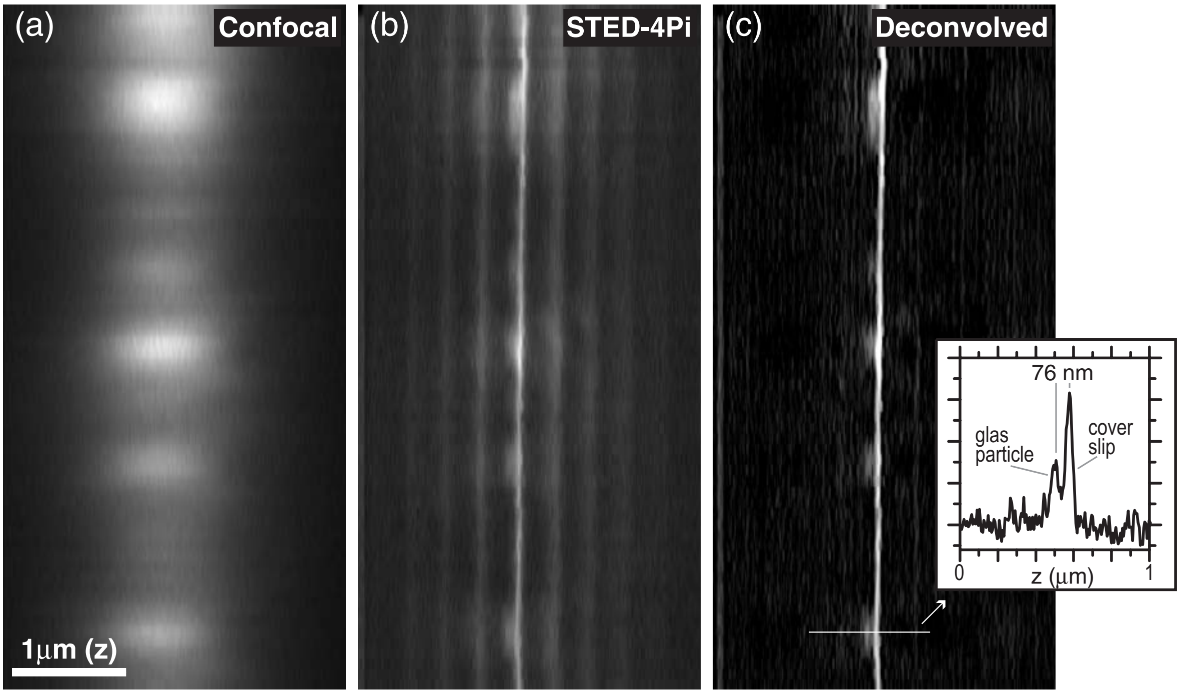

Figure 2.6: **Demonstration of the resolving power.** The image shows glass particles distributed on a cover slip. The glass surfaces were covered with Pyridine 2 by the adsorbtion effect out of a water solution. (a) is the confocal reference, (b) the STED-4Pi image, and (c) after a linear deconvolution step. It shows the substantial increase of the z-resolution, while the lateral one is unaffected.

in the frequency space. $\tilde{F}(h_{eff}(\vec{r}))$ is called the *optical transfer function.* The OTF is in fact a complex function including phase and amplitude information. However, in this work the OTF is refered to the modulus sqare $|\tilde{F}(h_{eff}(\vec{r}))|$ for simplicity. While the imaging process in space is described by a convolution of the object with $h_{eff}(\vec{r})$, in the frequency domain it is described by a multiplication of the OTF with the Fourier transform of the object (according to the Fourier theorem). Thus, an extended OTF means the ability to transmit high spatial frequencies from the real object to the image and therefore to resolve small structures. For a detailed introduction of that concept, see [17]. A comprehensive discussion of the OTF for most modern microscope techniques is published in [56].

The OTF of the STED-4Pi microscope can be calculated by evaluating $h_{eff}(\vec{r})$ in real space, as described in section 2.1. Finally, a numerical Fourier transform [63] reveals the OTF. For a STED microscope, its OTF depends in the same way on the dye used and STED parameters (intensity, wavelength, etc.) as the PSF [37]. For the case shown in Fig. 2.1, the corresponding OTF is calculated in Fig. 2.7(a). $k_u = 2\pi/u$ and $k_v = 2\pi/v$ are the spatial frequencies, where u and v are the normalized optical units, as defined in [80]. Part (b) shows the OTF of the confocal microscope, i.e. for $h_{STED} = 0$. The STED-4Pi OTF is substantially increased along k_u. Along the lateral frequencies, the OTF is mostly unchanged since the STED-4Pi microscope performs the confocal resolution in the lateral direction only. The profiles shown in the graph (c) show the enhanced frequency band in more detail. Which frequencies are useful depends on the signal-to-noise ratio of the image. In the present case,

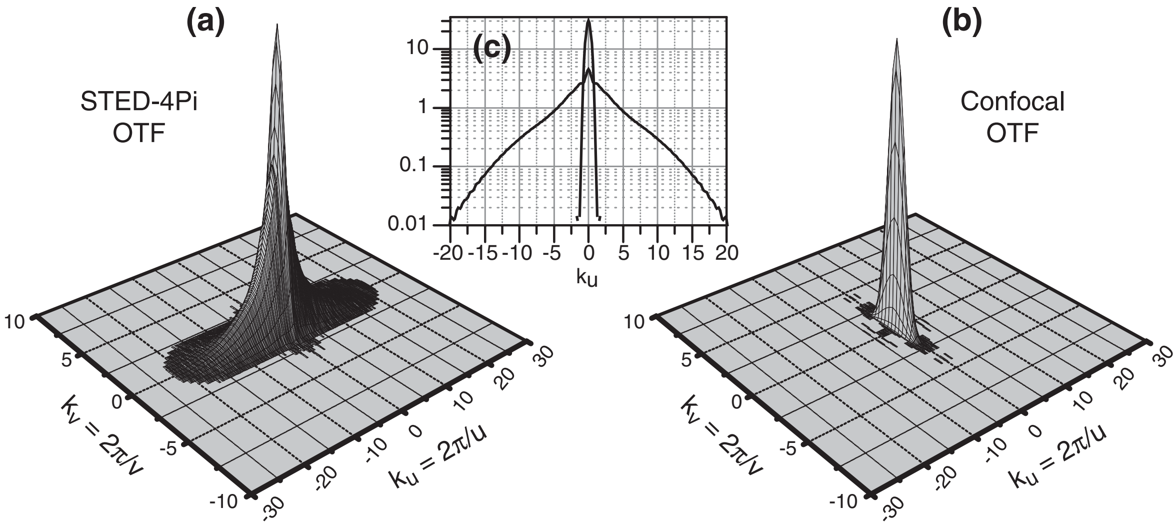

Figure 2.7: **OTF of the STED-4Pi** (a) **and confocal microscope** (b)**.** For (a) a two-zone aberration with $m = 0.4$ and $P = 0.37$ was assumed. (c) is a semi-log plot of the OTF at $k_v = 0$.

the STED-4Pi microscope features e.g. a five fold larger frequency band compared to the confocal one, if the noise level is about 3% of the signal, which can be seen as a realistic condition.

The OTF concept is also very useful for a discussion of artificially introduced phase functions $\Psi(\vartheta)$ (see Formula (2.2)). In Fig. 2.8, OTF for same conditions as for the PSF in section 2.1 are represented. In part (a), a two zone phase function with parameters $m = 0.4$ and $P = 0.37$ was used for h_{STED}. For comparison, in part (b), an unaberrated spherical wave ($\Psi(\vartheta) = 0$) was assumed. In the unaberrated case an oscillation behavior of the OTF in the k_u-direction occurs. This is related to the presence of residual side maxima in the PSF stemming from higher order minima in h_{STED}. (For each OTF, the correlated PSF h_{eff} is shown in the inset.) It can be understood by thinking about an object consisting of two points placed on the optical axis ($r = 0$) with a distance of the maxima in h_{eff}. While scanned through the PSF, both points will raise to a maximal signal at the same time. Thus, for a standing wave with an infinite number of equally intense side maxima this could not be distinguished from one point of doubled intensity. In this case, the OTF would have a complete lack at the corresponding spatial frequency $2\pi/\Delta z$, if Δz is the distance of the maxima. The same holds true for multiples of $2\pi/\Delta z$. Since the side maxima are not equally intense, the support of these frequencies is not vanishing, but strongly suppressed. Because the introduction of $\Psi(\vartheta)$ eliminates the side maxima, the correlated OTF (a) no longer shows the oscillations. Hence, $\Psi(\vartheta)$ produces a completely transmitted frequency band, largely enhanced compared to the confocal case. This becomes important for further nonlinear image restoration procedures.

The axial frequency bandwidth for the case of Fig. 2.8(a) therefore is slightly smaller than in (b). In other words, the axial FWHM of the PSF is larger. In fact, the PSF have a FWHM of 0.45 u with and 0.37 u without the aberrating phase function[12]. The reason is

---

[12] $u = (2\pi/\lambda) z n \sin^2\alpha$ is the optical unit; the values are equivalent to 45 nm and 37 nm for λ=745 nm and an oil objective with NA=1.4.

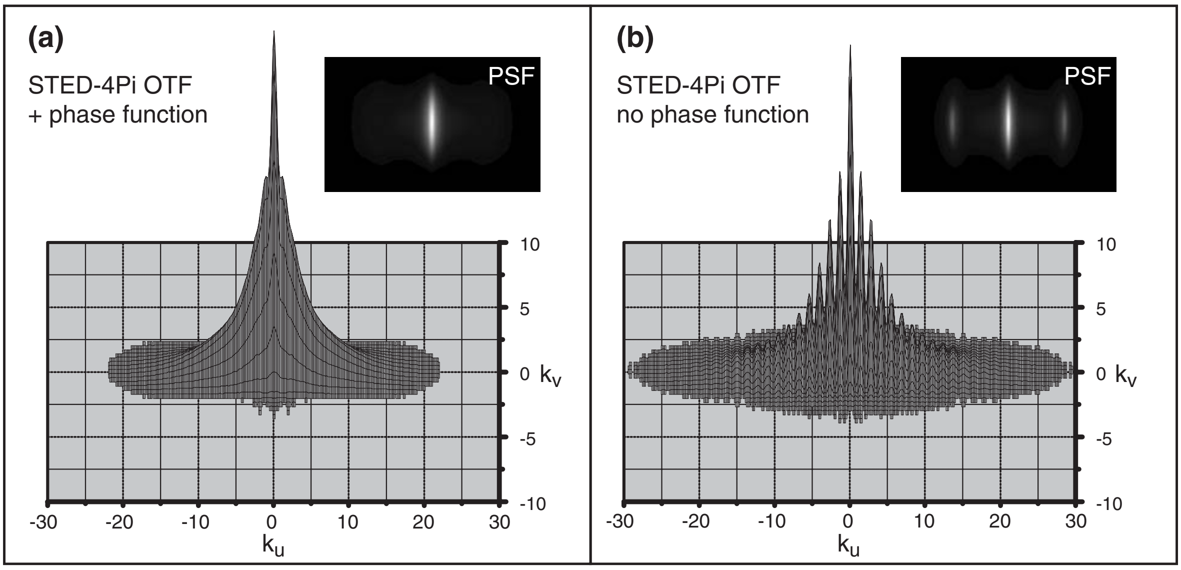

Figure 2.8: **Effect of a two zone phase filter on the STED-4Pi OTF.** Both OTF are calculated for the same STED parameter. In (a) the two-zone phase filter was applied, while in (b) the aberration-free situation is represented. The insets show the corresponding PSF.

that the phase function causes a slightly broader central minimum. So squeezing the central spot of excited molecules becomes slightly less efficient. This can be partly compensated by increasing the overall power of the STED beam.

The OTF properties of the STED-4Pi microscope can be experimentally verified by measuring an axial response V(z) and carrying out a Fourier transform along the optic axis. The result will here be called *1D-OTF* $\tilde{V}(k_z)$ and is given by $\tilde{V}(k_z) = \int \exp(-ik_z z) V(z)\, dz$. Data are shown in Fig. 2.9 for the confocal mode (a), as well as for the STED-4Pi mode with (b) and without (c) an aberration phase function. The axial responses $V(z)$ is shown at the left and the 1D-OTF $\tilde{V}(k_z)$ at the right. $\tilde{V}(k_z)$ was calculated by a numerical Fourier transform [63]. $V(z)$ was measured on a layer of Pyridine 2 molecules that had been adsorbed at the coverslip surface as in the previous experiments. The profiles were recorded with water immersion objectives (NA=1.2), excitation pulses with λ_{exc}=553 nm, and STED pulses with λ_{STED}=745 nm, τ=13 ps, and $max(h_{STED})$=2×10^{17} cm^{-2} in Fig. (b) and $max(h_{STED})$=1×10^{17} cm^{-2} in Figure (c). The phase aberration for panel (c) was achieved according to Formula (2.2) with $m = 0.56$ and $P = 0.57$ by a phase delaying MgF$_2$ coating. The primary effect on the 1D-OTF is a broadening of the frequency bands in Fig. 2.9(b,c) compared to the confocal reference (a), as predicted by the simulations. This is equivalent to the narrowing of the central peak in $V(z)$ and again proves that overcoming of the diffraction limit, since frequencies outside the diffraction bandwidth are present[13]. Furthermore, the oscillatory behavior of the aberration-free STED-4Pi microscope can be seen in the OTF of panel (b). The reduction of the side maxima and the concomitant fading of the OTF oscillation is demonstrated in Fig. (c). It underlines the importance of phase aberrating devices in STED-4Pi microscopy [26]. As in the previous measurements, the sidelobe effect does not completely vanish and

---

[13] In principle, even the confocal microscope transmits frequencies slightly above the diffraction range. This is due to the multiplication with the detection PSF of the point detector. However, the broadening in confocal microscopy still is in the order of a factor 1.

therefore a slight oscillation is still present in the right graph of part (c). But, importantly, the frequency transmittance in the former gaps is substantially increased. These frequencies are now more pronounced in the images. Note the systematical match of the experimental 1D-OTF of Fig. 2.9 with the corresponding simulations (Fig. 2.7, 2.8).[14]

---

[14] For comparison, $\tilde{V}(k_z)$ is represented in the OTF of the simulations by the profile line at $k_v = 0$.

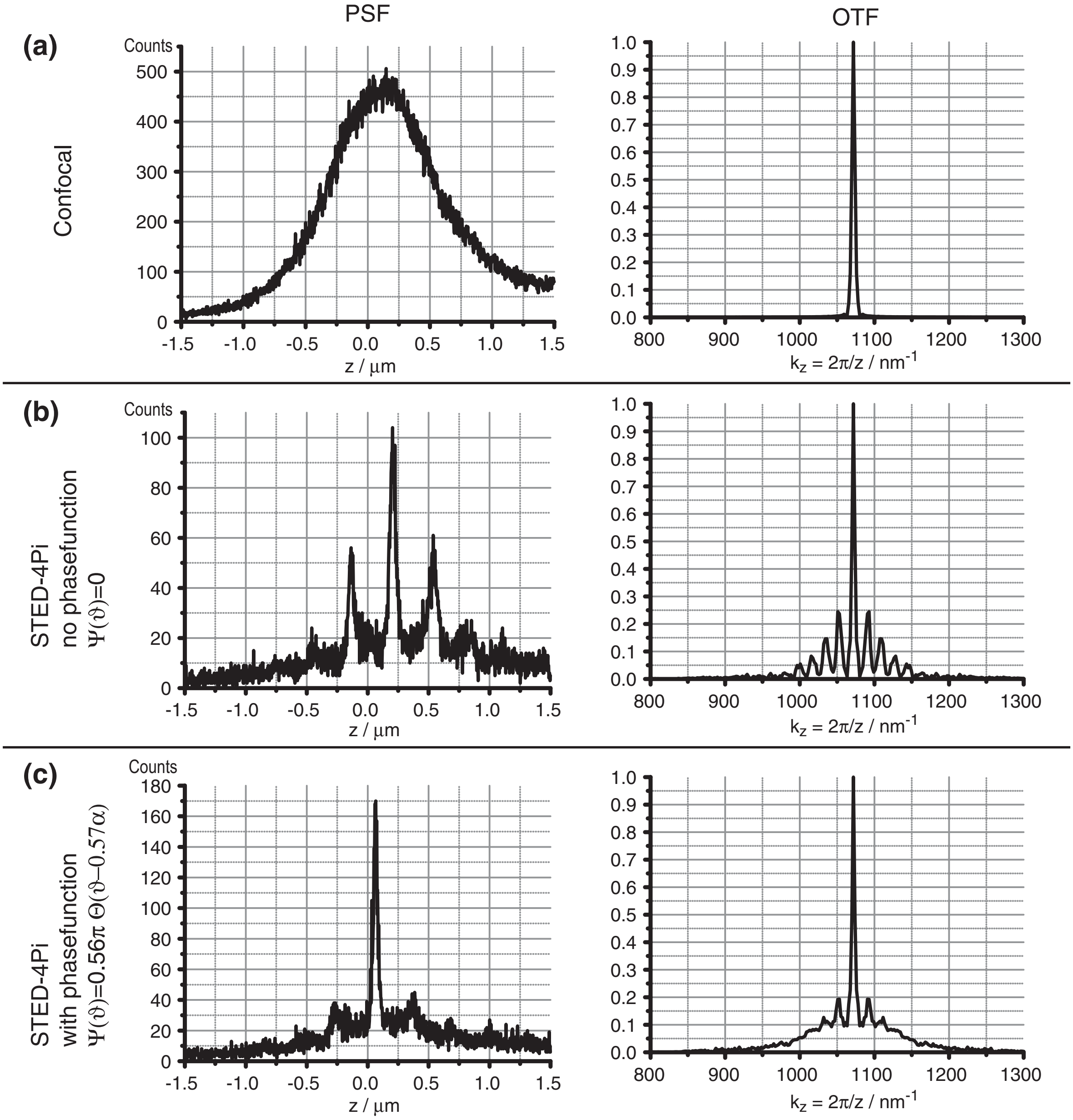

Figure 2.9: ***Z*-responses measured on a Pyridine 2 layer and 1D-optical transfer functions** deduced by a one dimensional Fourier transform for the confocal reference (a), the STED-4Pi microscope with no aberration phase function (b), and for the STED-4Pi microscope with a two zone aberration phase function of kind (2.2) with $m = 0.56$ and $P = 0.57$ (c).

Chapter 3

STED imaging of cell membranes

For STED microscopy with depleting pulses in the NIR regime, styryl pyridinium dyes generally turned out to have high STED supression $\eta(h_{STED})$ combined with low reexcitation by the STED pulses. Some of these dyes have a lipophilic behavior and can be used for in-vivo labeling of cellular membranes [38]. In this chapter high resolution images of membrane labeled bacteria are presented with the new STED-4Pi technique [8] and photostability is discussed for STED conditions in this biological environment [9]. It will be shown that a resolution of 33 nm can be reached in biological samples and that photobleaching by STED pulses is nonlinear. The photobleaching can be reduced by increasing the pulse length without affecting the depletion process.

3.1 Imaging of RH414 labeled *bacillus megaterium*

For a first biological application, the inner membrane of *bacillus megaterium* was labeled with the styryl-pyridinium dye RH414[1] [15]. For the preparation of the samples, see the Appendix. In the membrane environment this dye exhibits a fluorescence blue shift of 90 nm and a large increase of the quantum yield, as also known for very similar voltage-sensitive dyes [13]. The spectra are shown in Fig. 3.1(a). Laser lines at λ_{exc}=555 nm and λ_{STED}=760 nm were used for the experiments. The depletion curve is shown in part (b) for a STED pulse length of τ=13 ps. For comparison, the depletion curve of Pyridine 2 in water as used for simulations in section 2.1 is shown, too. RH414 depletion is less efficient, but can still be used for high resolution imaging. Fig. 3.2(a) is a standard confocal xz-image. It reveals that the confocal mode overemphasizes membrane regions oriented in z. One reason is that the dye molecules are oriented with their transition dipoles primarily perpendicular to the membrane [55] and parallel to the excitation field, if the membrane is plane to the optical axis. Another reason is the about 3-4 times elongated focal spot compared to the lateral direction. In the STED-4Pi microscope, the situation is reverted. According to the calculations in section 2.1, h_{eff} is now 4 times narrower in z. Thus, in the STED-4Pi image of Fig. 3.2(b), regions with the membrane aligned to the lateral direction are more strongly represented. Thus, the geometry of the focal spot has always be taken into account for image interpretation.

The main result, however, is a significant improvement of the axial resolution down to 40-50 nm in the raw data of part (b). The image also shows sidelobe effects. The reason for

---

[1] *N-(3-triethylammoniumpropyl)-4-{4-[4-(diethylamino)phenyl]butadienyl} pyridinium dibromide* (Molecular Probes Inc., Eugene, OR, USA)

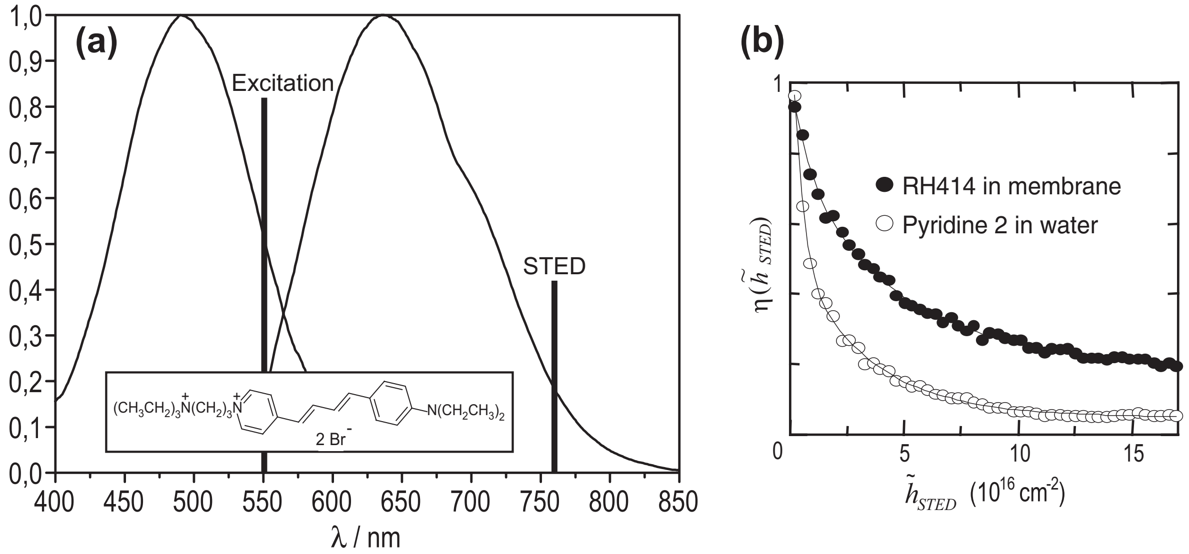

Figure 3.1: (a) **Excitation and Emission spectra** of the membrane incorporated dye RH414 and laser line positions chosen for the STED experiments. (b) **The depletion curve** $\eta(\tilde{h}_{STED})$ for RH414 in membrane and Pyridine 2 in water, for comparison.

their extended height compared to the Pyridine 2 experiments in non-biological samples is the less favorable $\eta(\tilde{h}_{STED})$ for RH414 molecules (see Fig. 3.1(b)). Again, the side maxima can be eliminated by a linear deconvolution filter [72]. The experimental $V(z)$ for the deconvolution was extracted from layer responses featuring the same lobe-height. The result is shown in Fig. 3.2(c). The profiles of the membrane show sharp peaks of 30 nm FWHM and a distinct separation of opposite parts of the bacterium.

The STED images were recorded with $max(h_{STED}) = 5.1 \times 10^{17}\,\mathrm{cm}^{-2}$, achieved by focusing 8.8 mW of time averaged power, which is in the typical range used in nonlinear microscopy, e.g. for two-photon excitation. The pixel integration time was 5 ms for the STED image and 2 ms for the confocal reference image. In all images the pixel dimension is 3.9×66 nm.

It should be mentioned that the xz-images as presented here would not have been possible with nearfield optics, that namely is not limited by diffraction, but inherently surface bound. In contrast, 3D sectioning with diffraction unlimited resolution along the optical axis needs freely propagating waves. Also, by applying an additional h_{STED} distributing the STED light in the lateral direction [39, 40], sub-diffraction resolution in the range of tens of nanometers should be available in all directions. This would eliminate structural overemphasizing by the spot geometry and therefore prevent misinterpretation of fluorescence images.

3.2 Photostability studies under STED conditions

With the system of RH414 in cell membranes, it is possible to reach resolutions of 30-40 nm. The limit is given by the applicable STED power, because of the imperfection of the central minimum $h_{STED}(\vec{r} = \vec{0})$ and of the onset of photobleaching. The first limitation could be optimized by controlling the focal aberrations, e.g. by adaptive optics. To understand the photodestruction limits, the dependence on the pulse energy, its duration and also on the

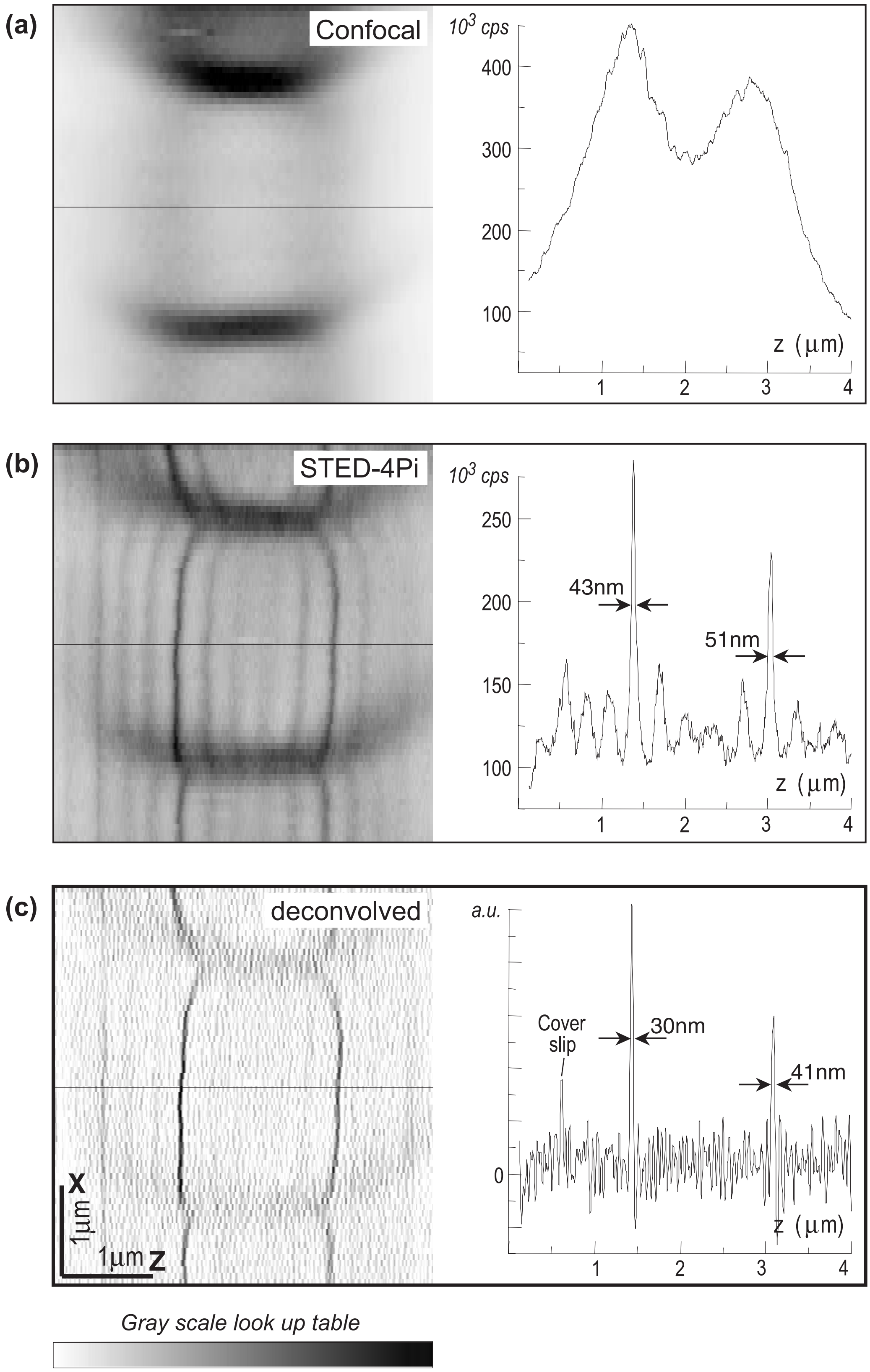

Figure 3.2: **XZ-cross sections of membrane-labeled bacteria.** (a) Confocal, (b) STED-4Pi and (c) STED-4Pi after linear filtering. In the right part, z-profiles along the black line in the images are printed. The STED-4Pi technique reveals novel far-field light microscopy images with 30-40 nm axial resolution. The confocal reference image was recorded by switching off the STED beam.

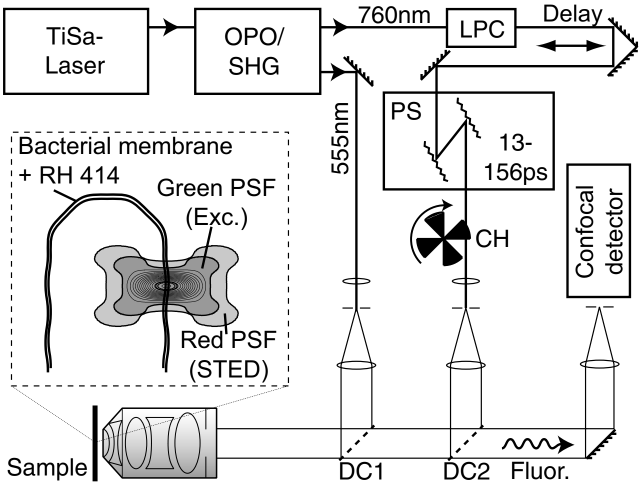

Figure 3.3: **STED-4Pi setup as used for the photo damage experiments** on fluorescence labeled bacterial membranes.

time order of the excitation and STED pulses is investigated in this section. The experiment were done under the same environment-specific conditions by recording fluorescence signals of RH414 labeled bacteria under the action of STED pulses with varying properties. Even if STED is the dominant process whith parameters chosen as in the previous section, further photophysical actions shall be investigated here, and under reverse order of arrival, the *STED pulse* does not perform stimulated emission at all. Therefore, in this section, the pulses with $\lambda = 760\,\text{nm}$ are referred to as the *red pulses*, and the excitation pulses with $\lambda = 555\,\text{nm}$ are named *green pulses*.

The bacteria were prepared as for the sub-diffraction measurements and placed in the focus of a water immersion objective lens (NA=1.2). The setup, as described in chapter 2, was used in confocal mode and was slightly enhanced, which is schematically sketched in Fig. 3.3. Time synchronized green pulses of ≈220 fs duration originating from the OPO and red pulses of primarily ≈120 fs from the Ti:sapphire laser are coupled via the dichroic mirrors DC1 and DC2 into the objective lens. Both laser beams are spatially filtered. The red pulses are passed through a liquid-crystal based power controller[2] to exactly control the pulse energies. To control the timing between the green and red pulses, the latter ones are propagating through a delay line of variable length by a motorized retro-reflector. Afterwards, the grating stretcher creates negatively chirped pulses of variable duration ranging from 13 to 156 ps that can be adjusted by the distance between the two gratings. Both laser beams are focused on the optic axis. Their focal spots are superimposed in space, the red focus covering the green one almost completely due to its larger extent (see inset of Fig. 3.3). An arbitrarily selected bacterium is placed in the common focus without spatial scanning. Thus, for the investigation of the photobleaching, fluorescence signals are recorded under certain laser pulse treatments on the same membrane spot for each measurement. The fluorescence was detected through DC1 and DC2 by the fiber coupled photodetector.

To enlighten the effect of pulsed laser light acting on the fluorescent compounds, the only observable measure in a light microscope is the implication on the fluorescence signal.

---

[2] *LPC-NIR* (CRI Inc., Woburn, MA, USA)

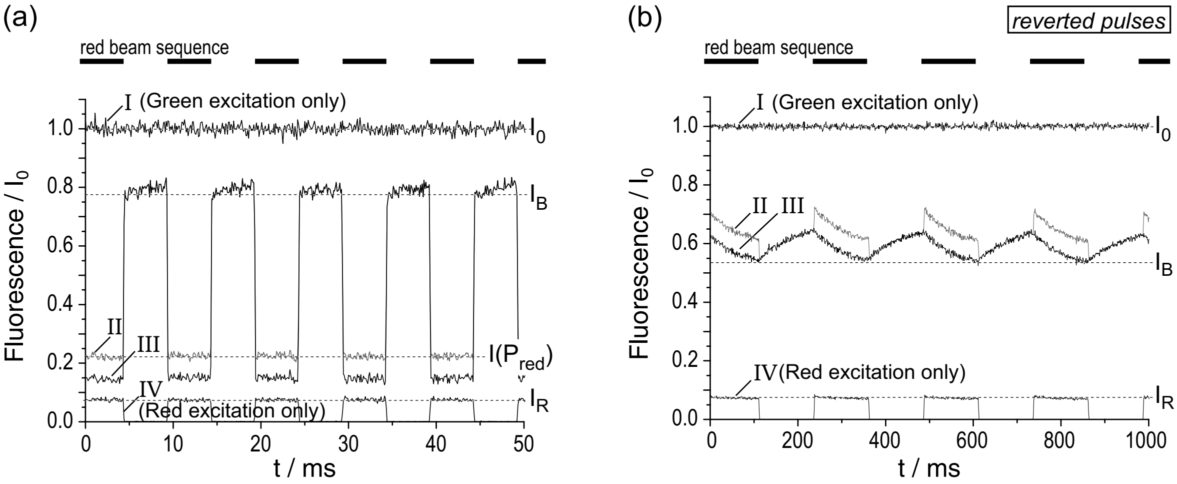

Figure 3.4: **Exemplary fluorescence traces** recorded in synchrony with the chopper wheel in the red beam. In (a) the red pulses are succeeding and cause STED as the main effect. In (b) the pulse order is reverted, so that no STED can happen. In both cases photobleaching is present, demonstrating that photodestruction does not happen from the excited state.

If the red pulses are following the green ones by a delay of some tens of picoseconds, the molecules that are excited by the green pulse are staying in the vibrational ground state of the electronically excited state S_1 (see 1.2). Then the red pulses are able to induce stimulated emission back to ground state, as needed for STED. Since this happens on a picosecond timescale, and the cycling time of the f=76 MHz laser system is $1/f$=13 ns, each molecule treated in this way is ready for a new excitation by the next green pulse. Thus, the hallmark of STED is an instantaneous change of the fluorescence signal in precise synchronisation with an energy modulation of the red pulses. Especially, if the red beam is interrupted, the complete fluorescence signal has to recover without delay.

This is different if the red beam additionally acts photodestructively. Photodestruction, in this sense, means any manipulation of the molecules that prevents them from exhibiting fluorescence emission for a long time, or even forever. Such a process would lead to a decreasing amount of intact molecules in the focal area. After interruption of the red beam, the fluorescence would recover with a temporal delay, since it is achieved by diffusion of new molecules into the focus, or additionally by a back-transition of molecules from a dark state (depending on the photodestructive process). The recovery would occur on a time scale given by the diffusion rate, or faster if additional recovery from dark states is present. So far, a secure method to distinguish between STED and other light driven manipulations is to look on the fluorescence recovery time after blocking the red beam.

For the experimental implementation, a chopper wheel was placed in the setup (see Fig. 3.3) and the fluorescence detection was triggered in synchronisation with its rotation. The switching time was faster than $100\,\mu s$ that is faster than the typical diffusion times inside membranes. Typical records of fluorescence traces are shown in Fig. 3.4. Panel (a) shows a measurement for succeeding red pulses, consisting of three recorded signal traces. Trace I is recorded initially after choosing a new spot on an arbitrarily chosen cell. It establishes the reference level I_0 of the membrane. At an applied time averaged power $P_{green} = 100 - 300\,\text{nW}$, photobleaching by the green excitation pulses is negligible within the time of observation. Type

II traces are detected under action of both pulses, after reaching equilibrium conditions. To correct for the residual excitation of the red beam, trace IV was recorded in absence of the green pulses. While the chopped red beam is blocked, the signal reveals the background signal of the microscope, which is negligible here. The presence of red pulses in IV reveals the level of residual excitation, I_R. Traces of type III are obtained by subtracting trace IV from trace II (III=II-IV). They are devoid of residual excitation by the red beam.

The data shown in Fig. 3.4(a) were detected with 13 ps red pulses following the green ones. This situation is the same as for the sub-diffraction measurements in section 3.1. Here, an average power $P_{red} = 3.67\,\mathrm{mW}$ was applied. In this case, STED is the dominant process. This can be seen by the fast switching of the fluorescence in trace II from level $I(P_{red})$ to I_B. $I(P_{red})$ is the level under STED, that depends on the power of the red beam, of course. I_B is the signal, that is obtained directly after blocking the red beam. For quantification, we define

$$\eta_{gross}(P_{red}) = \frac{I(P_{red})}{I_B} \tag{3.1}$$

as the *gross STED suppression coefficient*. It is related to an experimental point of view, since it describes the modulation of fluorescence caused by the red beam (involving its own excitation performance I_R). From a more physical point of view, the quantity

$$\eta_{STED}(P_{red}) = \frac{I(P_{red}) - I_R}{I_B} \tag{3.2}$$

with correction for residual excitation I_R through the red pulses describes the properly (*net*) STED suppression coefficient, since it depicts the modulation just caused by stimulated emission. For an ideal STED system without any excitation probability by the red beam, it is $\eta_{gross} = \eta_{STED}$. The value of η_{STED} can be derived from the fast modulation at the rising edges of trace III.

A major finding of the experiments, as in Fig. 3.4(a), is that the signal I_B is not of the same height as the reference I_0. This indicates that beyond the stimulated emission, further manipulation of the molecules is present in a photodestructive way. Consistent with this finding, after switching off the red beam by the chopper wheel and reaching level I_B, trace II (and also III) exhibits a weak and slow signal increase with a time constant of ≈45 ms. This is due to the diffusion of unaltered molecules into the focus and – potentially, but not known – further back-transitions of previously altered compounds. Since a detailed analysis of that circumstance is the primary goal, we also quantify this by introducing the *bleaching efficiency*

$$\beta(P_{red}) = 1 - \frac{I_B}{I_0} \tag{3.3}$$

for the following discussion. $\beta = 0$ indicates an ideal STED system without further photophysical processes induced by the red beam. In contrast, $\beta = 1$ would indicate conditions useless for STED microscopy. For Fig. 3.4(a) it is e.g. η_{gross} =0.45, η_{STED} =0.39, and β =0.22.

An important observation was made by inverting the time order of both pulses, also referred to as *"reverted pulse order"*. An exemplary set of traces is depicted in Fig. 3.4(b), which was obtained under same conditions as in panel (a), except for the pulse timing. The average power P_{red} was 3.51 mW in this case. The traces I-IV have the same meaning as before. However, STED is no longer present in traces II and III. This is because the red pulse arrives directly

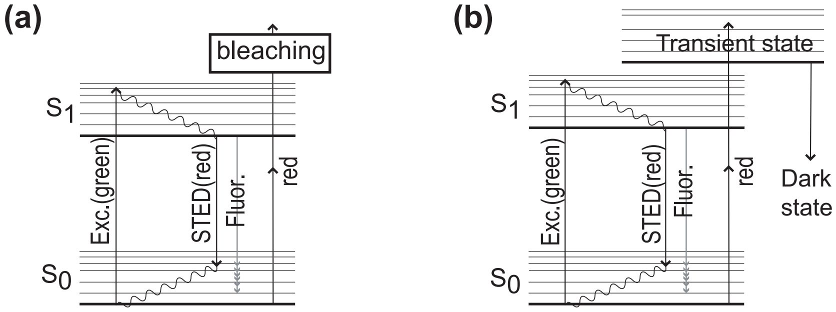

Figure 3.5: **Energy schemes for bleaching mechanisms** that are consistent with the data. (a) Most likely, detrimental effects are initiated from the ground state, S_0. (b) Alternatively, photo bleaching can also be mediated from an intermediate state with a lifetime longer than the pulse cycling time, e.g. a triplet state or a conformational change of the compounds.

before excitation by the green pulse happens. Thus, except from residually excited molecules by the red pulse itself, the red pulse arrives at the sample when no molecules are in the excited state. This is ensured because the pulse cycling time of $1/f$=13 ns is much longer than the measured fluorescence lifetime of τ_{fl}=1.37 ns of RH414 inside the membrane. Thus, no excited molecules are present from previous excitations. The signal created by the succeeding green pulse is proportional to the number of intact molecules in the focus. For an ideal system, trace III should not be different from trace I. However, for the present system, the red pulses cause a distinct modulation of the fluorescence in antisynchrony with the chopper wheel. During treatment with the red beam, the signal decreases slowly and recovers during the blocking period. The signal again does not reach the reference I_0. The conclusion is that the red pulses cause a detrimental effect also without preceding excitation. With high probability, this effect is initiated from the molecular ground state, S_0. A build up of a S_1-population can be excluded as discussed above ($\tau_{fl} < 1/f$). Higher singlet states S_n decay even faster with time constants in the picosecond range (Kasha's rule) [36, 68]. Therefore photodamage either starts directly from S_0 or is mediated by a long-living intermediate state, such as a triplet sate, or a conformational change of the molecule structure. Furthermore, reverted pulse measurements indicate that alone the red pulses are responsible for the photobleaching. This seems to become evident by the fact, that variation of P_{green} does not have an effect on the amount of photodestruction (data not shown). Possible bleaching schemes that are consistent with the data are shown in Fig. 3.5.

By now, only one set of traces for normal and reverted pulse order was presented and quantities η_{gross}, η_{STED}, and β were introduced for further analysis. Even if some properties of the photodestructive mechanism could be clarified, important conclusions can be drawn by recording sets of traces for different average powers P_{red} (while pulse length τ_{red} is fixed) and by varying τ_{red} (while P_{red} kept fixed). For reverted pulses, four traces for a constant power (P_{red}=5.52 mW) and pulse durations τ_{red}=13, 40, 85, 156 ps are shown in Fig. 3.6(a). Hence, all curves represent photodamage for the same pulse energy of 72.6 pJ, but with different pulse peak intensities of 906, 313, 147, and 80 MW/cm^{-2} in the center of focus, respectively. At constant pulse energy and repetition rate, the probability of a multi-photon process of order n scales with τ_{red}^{-n+1}. The traces in Fig. 3.6(a) reveal a strong increase of the fluorescence modulation, as well as a decrease of the average fluorescence level for decreasing τ_{red}. For a

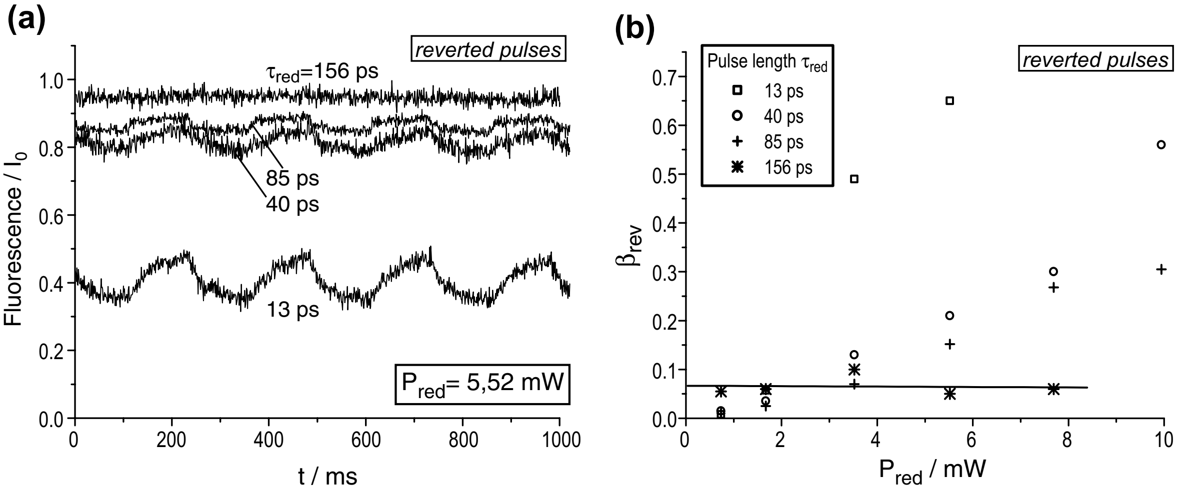

Figure 3.6: **Photobleaching with reverted pulse order for different parameters of the red pulses.** (a) Background corrected traces of type III recorded with varying pulse durations τ_{red} for a fixed average power P_{red}=5.52 mW. The curves are normalized to the corresponding reference level, here set as $I_0 = 1$. The shorter τ_{red}, the stronger is the photodamage. For τ_{red}=156 ps, nearly damage free conditions are obtained. (b) Bleaching level β_{rev} over the average power P_{red} is shown for different τ_{red}. The dependence on both parameters can only be explained if the damage is nonlinear, i.e. caused by multi-photon absorption.

single-photon process it is n=1 (normal absorption of a photon) and no dependence on τ_{red} would be observed. Therefore the damage is nonlinear ($n \geq 2$), i.e. caused by (at least a major component of) multi-photon absorption. Note the strong signal reduction for τ_{red}=13 ps. For τ_{red}=156 ps, fluorescence reaches 96% of the reference level I_0, meaning nearly bleaching-free conditions.

In panel (b) the bleaching index for reverted pulses $\beta_{rev}(P_{red})$ (defined by Formula (3.3)) is shown as a function of the average power of the red beam for 13, 40, 85, and 156 ps pulses. This diagram underlines the strong dependence of the photodamage on the peak intensity of the red pulses. For 13 ps pulses β_{rev} reaches ≈0.65 in the investigated range up to P_{red} ≈6 mW[3]. For increasing pulse durations, bleaching becomes less efficient. For 156 ps long pulses, the bleaching keeps almost constant at β_{rev} ≈0.06 in the observed range up to ≈8 mW (see line in panel Fig. 3.6(b)).

Since STED is a single-photon process ($n = 1$), no pulse length dependence on the STED suppression exists in the range $\tau_{vib} \ll \tau_{red} \ll \tau_{fl}$ as long as P_{red} is kept constant (see Formula 1.2). Here, this becomes crucial for unscrambling STED from photobleaching. Tuning τ_{red} to large values, while maintaining $\tau_{red} \ll \tau_{fl}$, STED should remain pronounced, while photobleaching decreases at least for the system under investigation. The insensibility of STED against the pulse duration can be experimentally verified by changing the pulse order back to succeeding red pulses and analyzing η_{STED} and η_{gross} for different pulse durations. This is shown in Fig. 3.7(a,b), where $\eta_{gross}(P_{red})$ and $\eta_{STED}(P_{red})$ are depicted again for pulse

---

[3] At a repetition rate f=76 MHz, the average powers of P_{red}=6 mW corresponds to a pulse energy of 79 pJ. Focused by an objective lens with NA=1.2 and spread over 13 ps (assuming rectangular pulses) this leads to a pulse peak intensity of 1 GW/cm^{-2} in the focal center.

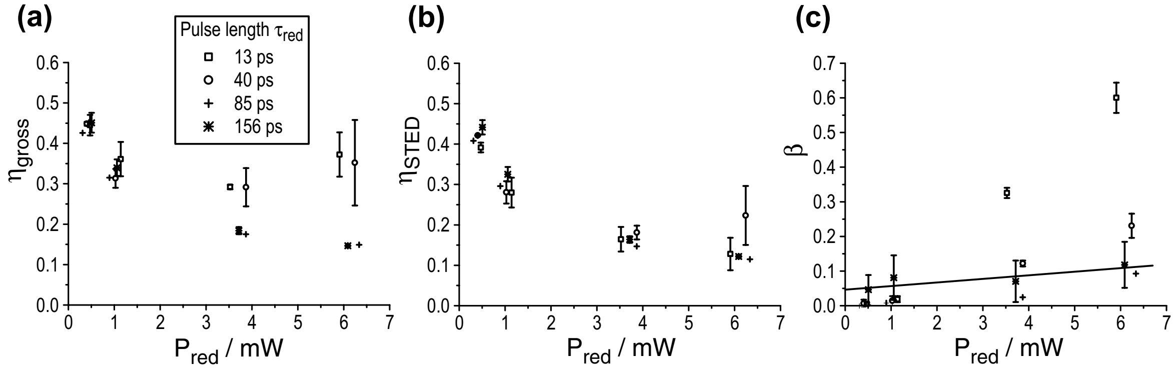

Figure 3.7: **Suppression coefficients** (a) η_{gross}, (b) η_{STEDs} **and** (c) **bleaching index** β for normal pulse order under varying parameters of the red pulses. In panel (a) the depletion rate is effected for short pulses by residual excitation of the red pulse. Since the reexcitation rate depends on τ_{red}, it is due to multi-photon excitation. After correction for this reexcitation, panel (b) proves the independence of STED on the pulse length in the range from 13 to 156 ps. (c) shows the bleaching index β for the same pulse parameters and reveals again its nonlinear behavior.

durations of 13, 40, 85, and 156 ps. At comparatively low values of P_{red}, η_{gross} does not vary within the the span of pulse durations. Above ≈4 mW, the depletion curve increases for short pulses of 13 and 40 ps due to reexcitation by the red pulses. In this case, reexcitation excels the effect of further fluorescence suppression by STED. For longer pulses, however, this effect is not pronounced. Since the residual excitation from red pulses depends on the pulse length, it has to be caused by multi-photon excitation that can be eliminated by choosing longer pulses. The data presented in Fig. 3.7(b) are corrected for reexcitation. It can be clearly seen that the suppression coefficient η_{STED} indeed is independent from τ_{red}, within the range of error bars, which are deduced from multiple measurements repeated on different membrane spots. As expected from the theory, the physical process of STED, described by η_{STED}, depends only on the pulse energy, i.e. the number of photons contained in a pulse. The experimental $\eta_{STED}(P_{red})$ of Fig. 3.7(b) enrolls the saturation behavior of STED by an exponentially increasing efficiency of fluorescence suppression with increasing stimulating power.

The concomitant effect of bleaching is illustrated in Fig. 3.7(c), where the bleaching index β is depicted. Consistent with the findings for reverted pulse order, bleaching depends strongly on τ_{red} and reaches again $\approx \beta = 0.6$ for 13 ps pulses at a power of 6 mW. It also shows that within the investigated power range that photobleaching remains virtually constant at a low level for long pulses of 156 ps (solid curve in Fig. 3.7(c)).

In summary, it could be proved that all side effects caused by the STED light are nonlinear, i.e. caused by multi-photon absorptions. This holds true for both cases, photobleaching and reexcitation. Following from reverted pulse order experiments, it seems most likely that photobleaching is initiated from the ground state of the molecules, or perhaps from a long-living intermediate state. The multi-photon characteristics of the detrimental action could be proved by the bleaching indices β_{rev}, β under reversed pulse order as well as under STED conditions. A signal reduction through photodestruction could be widely minimized by the use of pulses >100 ps. The process of stimulated emission was unaffected by the pulse length, since it is a single-photon effect. This could be proved by measuring η_{STED} for different pulse durations over more than a order of magnitude. Fortunately, the residual excitation of molecules through the red pulses is due to multi-photon excitation and could be minimized by the use of long pulses too. At least for the present system of membrane incorporated RH414, the choice of pulses ranging from ≈150 ps to approximately half of the excited state lifetime enables highly efficient STED by simultaneous reduction of the undesirable effects of the STED pulses. The finding that photobleaching has a nonlinear origin is generally consistent with other investigations of photobleaching under treatment with ultrashort laser pulses [32], and is also a limiting factor in two-photon excitation fluorescence microscopy [43, 34, 59]. In this mode of microscopy, photodestructive two-photon absorption can be unscrambled from two-photon excitation only by the choice of wavelength, since both have the same pulse length dependence. As explained, this is different for STED as a linear process. For example, a three fold improvement of resolution above the diffraction barrier is achieved by a pulse energy of ≈ 120 pJ focused by a high numerical aperture lens. This is quite precisely the typical energy used in a two-photon microscope. Because for STED ≈3 orders of magnitude longer pulses are used[4], parasitic nonlinear effects are suppressed by 3 and 6 orders of magnitude for two- and three-photon effects, respectively. This also means that the applied peak intensities are live-cell compatible and far below nonlinear damage thresholds for live mammalian cells [42].

---

[4] 150 ps for STED compared to 150 fs for two-photon microscopy

Chapter 4

Immuno-fluorescence STED imaging

The work presented so far demonstrates the ability of the synergistic combination of STED and 4Pi-microscopy to obtain axial resolutions of some tens of nanometers with non-biological samples and bacteria whose cell membrane was labeled with a styryl dye. The recording of the bacterial samples was enabled by the use of water immersion lenses, which is an inevitable step forward to further biological applications. However, the realization of more advanced biological STED applications remained unclear at first. A major reason is that STED-functional dyes used up to now were not functional as biological markers, except for some lipophilic styryl pyridinium dyes. They were useful as membrane markers for selected structures, e.g. for prokaryotic cell membranes (Chapter 3) [38, 8]. Thus biological STED imaging was limited to membranes. The membrane environment may have a protective influence on the photostability, even if photobleaching is present under treatment with short STED pulses in the case of RH414. In this chapter, a red emitting dye capable for STED is presented. It can be efficiently depleted around λ_{STED}=785 nm in an aqueous, bio-compatible environment and is functionalized for standard immuno-fluorescence preparations. High resolution STED images of the immuno-labeled microtubular network of human embryonic kidney (HEK) cells are shown. They have a 15 fold improved axial resolution compared to a standard confocal scan. Additionally, a lateral resolution of ≈100 nm could be achieved within the same setup by the use of a single beam technique with annular phase filters. For these results, further improvements in the experimental setup were necessary which are described in the first section. The results demonstrate that a 3D-superresolution of at least 100x100x50 nm can practically be realized in immuno-fluorescence imaging. Major results of this part of the thesis are published in [10].

4.1 Improvement of the STED-4Pi setup

While the results presented so far verified that STED can provide axial superresolution at least about 15 times better than confocal resolution, the long-term objective is a STED microscope that affords superresolution in all directions. For lateral resolution improvements, several principles were already presented [41, 39, 40]. They all use a single STED beam focused through one objective lens of a confocal microscope. The most powerful variants are based on annular phase filters. They modify the incident wavefront to form a focal light distribution with a central minimum and surrounding maxima. The integration of an additional (single) STED beam into the STED-4Pi microscope becomes possible by the use of a polarization controlled

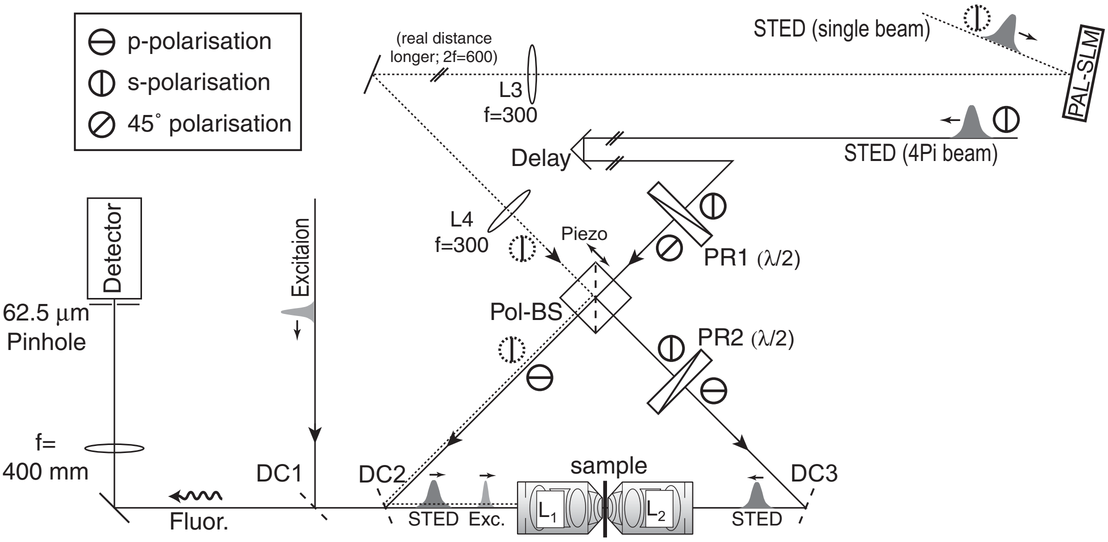

Figure 4.1: **Improved setup of the STED-4Pi microscope** as used for the immuno-fluorescence imaging. A polarization controlled 4Pi-cavity and a 532 nm mode-locked laser for excitation were implemented.

4Pi-interferometer. It allows the simultaneous application of a STED-4Pi beam propagating through both interference arms as well as a STED beam passing only into the objective lens that is used for excitation. Wavefront modulation of the latter one will allow simultaneous lateral resolution enhancement.

A sketch of the modified STED-4Pi setup is represented in Fig. 4.1. The 50% beamsplitter (BS) of the 4Pi-interferometer (see Fig. 2.2) is replaced by a polarization beamsplitter (Pol-BS) reflecting vertical and transmitting horizontal polarization, respectively. The STED-4Pi beam is rotated to 45° polarization by a $\lambda/2$ phase retardation plate (PR1). Half of the light (horizontal polarized) passes into the left interference arm, while the other half is reflected into the right arm. Its vertical polarization is rotated by 90° by a second $\lambda/2$ phase retardation plate (PR2), so that both beams can interfere in the focus. While at first look this setup seems to be more complicated, it allows in fact a much more precise control of the STED beam parameters. Rotation of PR1 allows precise equalisation of the beam intensities, while PR2 enables exact matching of the polarization directions. Optimization of both parameters is crucial for a maximal interference contrast and therefore for reducing residual intensity at the central minimum. As discussed in Chapter 2, this is important for ultimate saturation levels of the depletion beam.

The additional lateral STED beam can now be supplied through the fourth edge of the beam-splitter (Pol-BS) with vertical polarization. It passes into the objective lens L_1 that also is used for excitation. The additional STED beam is first expanded by using a spatial filter and a f=200 mm collimating lens (not shown). It is reflected from a liquid crystal based spatial light modulator (PAL-SLM)[1] that modulates the phase distribution of the incident beam. The phase pattern of the PAL-SLM is reproduced at the entrance pupil of the objective lens L_1 by a 4-f optics (lenses L3, L4; f=300 mm). The timing of the pulses from both STED beams is

---

[1] *PAL-SLM* (*parallel aligned liquid crystal spatial light modulator*; Hamamatsu Photonics Deutschland GmbH, Herrsching, Germany)

adjusted by a delay line in the STED-4Pi beam path.

So far, the microscope can be used for axial superresolution by the horizontal polarized STED-4Pi beam, and for lateral superresolution by the vertical polarized single STED beam. Both STED beams have perpendicular polarization, while STED is most effective for parallel polarization of the excitation and STED light [16, 11, 46]. This is due to the fact that the transition dipole of a fluorophore in the ground and excited state basically have the same orientation. A linear polarized excitation beam excites those molecules in favour that are orientated parallel to the polarization. The same holds true for the depletion process that becomes most efficient if excitation and depletion polarization are set parallel. This effect, of course, can be influenced by molecular rotation between the excitation and depletion process. To achieve high efficient STED by both depletion beams, the excitation light can be 45 degree to both STED beams. Another possibility is to convert all beams to circular polarization directly in front of the objective lenses. Retrieving of high STED efficiency - as in the case of parallel polarization - becomes possible by increasing the applied STED power, if not compromised by extended photobleaching. However, for sequential recording with each STED beam, the excitation light should be turned parallel to the depletion light in use.

A further topic is the available STED power needed for the additional single STED beam. The gain of more laser power also would allow better spatial filtering to achieve better wavefronts. Especially for the single STED beam, a high quality wavefront is crucial to achieve an unaberrated STED-PSF with vanishing central intensity. Until now, the OPO used as the excitation source was pumped by the Ti:sapphire laser. As a consequence, the power of the STED beam was decreased, since about half of the light was converted in the OPO. In order to gain more STED light, the OPO was replaced by an independently working diode-pumped solid state laser[2]. This GE-100 laser originally had a repetition rate of f=120 MHz. For synchronization with the Ti:sapphire laser working at 76 MHz, it had to be redesigned. A f=76 MHz laser cavity was built as part of this work in collaboration with *Time-Bandwidth Products, Inc.* The laser produced 10 ps mode-locked pulses at 1064 nm that were externally frequency doubled. For phase stable synchronization of the GE-100 with the Ti:sapphire laser, the latter was driven by a piezo controlled cavity feedback system[3] , that locks the Mira-900F to a master clock signal, in our case produced by a trigger photodiode from the GE-100. Both pulse trains could be phase-locked with a jitter of <1 ps. The relative timing of both pulses can easily be adjusted by a control voltage applied to the Synchrolock directly from the control computer of the microscope. The spatially filtered excitation beam is coupled into microscope via the dichroic filter DC1 and passed through DC2 into the objective lens L_1. The fluorescence is detected in epi-fluorescence mode as already shown in Fig. 2.2. Other elements of the microscope, which are not mentioned here, remained unchanged as described in Chapter 2.2.

4.2 STED dye MR-121SE for immuno-labeling

Up to now, a broad basis of applications was limited, because useful STED dyes were not able to bind chemically on the structures of interest. Fortunately, properties like the adsorption of Pyridine 2 on glass surfaces and the lipophilic behavior of some dyes enabled imaging of selected structures. In collaboration with Prof. Drexhage (Department of Chemistry, University

---

[2] *GE-100* (Time-Bandwidth Products Inc., Zurich, Switzerland)

[3] *Synchrolock* (Coherent Inc., Santa Clara, CA, USA)

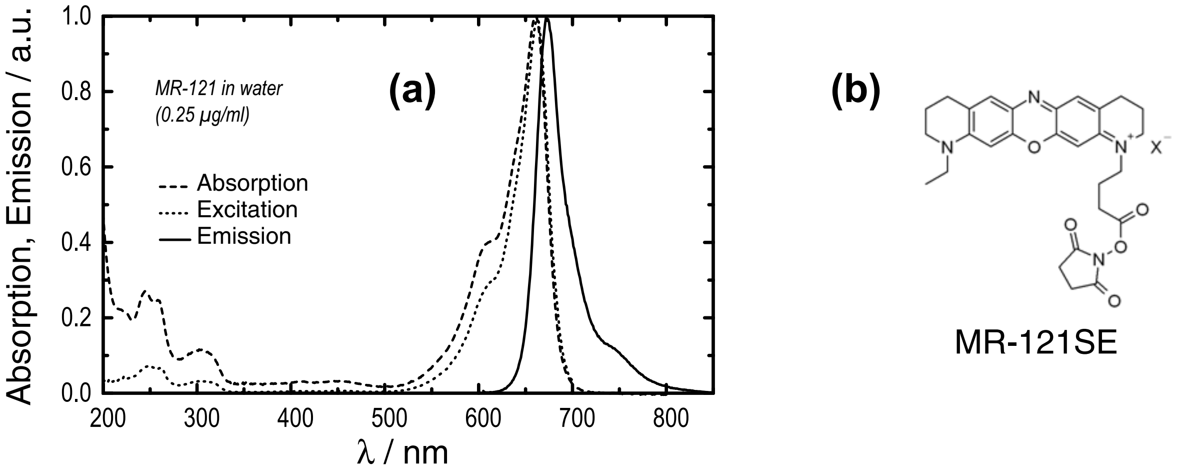

Figure 4.2: (a) **shows absorption, excitation, and emission spectrum of MR-121 in water, and** (b) **its chemical structure.**

of Siegen), a series of red emitting fluorescence dyes were screened for good STED properties under depletion with stretched NIR-pulses of a Ti:sapphire laser. Further requirements were the presence of a functional group to allow covalent binding to antibodies and other structures, as well as a good performance in water. A molecule that widely fulfilled this need is the oxazine derivate MR-121SE (supplied by Prof. Drexhage). The spectra and structure are shown in Fig. 4.2. The dye molecule exhibits fluorescence around 670 nm with an extended shoulder reaching up to ≈800 nm. It is functionalized with a succinimidyl ester group. This group can be covalently coupled to amino-groups, i.e. this dye is ready for antibody-labeling, as used for standard immuno-fluorescence preparations. In addition, the fluorophore is stable in water with a fluorescence lifetime of τ_{fl}=2.4 ns.

STED can be performed efficiently in the range $\lambda_{STED} \simeq$785-800 nm. For shorter wavelengths, the dye is excited by the STED pulses due to its comparatively small Stokes shift. The reexcitation decreases quickly above ≈780 nm. Even, if excited with 532 nm as in these experiments, the peak absorption at 661 nm is optimal for excitation with picosecond pulsed laser diodes at 660 nm [73, 78]. This is a cost efficient variant interesting for commercial purposes. Such diode was available for the last measurements in this Chapter which allowed a more efficient excitation.

A major advance is the ability to produce monolayers of MR-121 on the coverslip surface (see the Appendix). This is important because the STED-4Pi microscope necessarily needs to be readjusted after any sample change. The precise position of the objective lenses has to be aligned as well as the relative phase of both counter-propagating STED beams. For that purpose, a simple structure like a thin layer of a STED capable dye, is needed inside the sample. This is different from other types of STED microscopes since it is related to the 4Pi-adjustment. In one- or two-photon excitation 4Pi-microscopy, embedded fluorescent layers or microspheres are produced with standard fluorophores, or are available commercially. Due to the specific requirements on the fluorophores for STED microscopy, a standard layer could not be produced up to know. The adsorption of pyridine 2 worked only out of a watery dye solution and can not be used in general. Fortunately, the membranes themselves could act as layers for the adjustment.

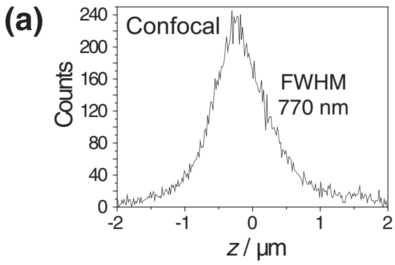

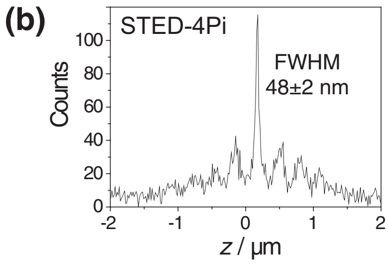

Figure 4.3: (a) **Confocal and** (b) **STED-4Pi z-response** of a monolayer of MR-121SE measured in an aqueous environment. The molecules were covalently bound to a silanized coverslip surface. Excitation was performed with 10 ps pulses at 532 nm. Although the molecules were excited below the absorption peak, an intense signal could be produced wit 10 μW average power. STED pulses with λ_{STED}=793 nm, stretched to τ=107 ps, were focused to a photon density of $max(h_{STED}) = 1.25 \times 10^{18}\,\mathrm{cm}^{-2}$ at the central peaks of the PSF. The profiles were recorded with 1 ms pixel dwell time and a pixel step size of 9.5 nm.

Now, the MR-121 monolayers can be easily used to record z-responses $V(z)$. Fig. 4.3 shows axial scans through a labeled coverslip surface in the confocal (a) and the STED-4Pi mode (b). Between the coverslips, water was placed and the data were recorded with water immersion objectives. The profile of Fig. 4.3(b) demonstrates a resolution performance under cell-free conditions of 48 nm, 16 fold improved compared to the confocal reference. $V(z)$ is used for a linear deconvolution step of the biological images in the next section to eliminate side maxima of the effective PSF, h_{eff}. The relative height of the side maxima compared to the central peak is <25%.

4.3 Microtubules of mammalian cells at 50 nm axial resolution

The amino-reactive dye MR-121SE can be used for immuno-labeling via a secondary antibody. We labeled the microtubular network of human embryonic kidney cells, which is difficult to resolve in 3D by a light microscope. The labeling was done according standard procedures (see the Appendix). One of the coverslips was covered with a MR-121 monolayer (see the Appendix). If recorded above or beneath the cell, it discloses the microscope's axial resolution under realistic sample conditions. The microtubular network consists of small tubes of $\alpha-$and $\beta-$tubulin with a diameter of $\approx$25 nm, while the labeled tubulus has an increased diameter of $\approx$ 60 nm [77]. A schematic tube decorated with the fluorescently labeled secondary antibody is shown in Fig. 4.4(a). The tubules are strongly reticulated, as can be seen in the confocal wide field overview in Fig. 4.4(b). Especially in the axial direction, this network is hard to resolve with a confocal microscope. To demonstrate the resolution obtained in immuno-fluorescence imaging, sections parallel to the optic axis (xz-images) were recorded. A typical cell is shown in Fig. 4.4(c,d). Panels (e) and (f) show the corresponding profiles along the marked lines in the images. In image (c), the STED beam was blocked to record in the confocal mode. Image (d) is the STED-4Pi counterpart of the same side of the cell, performed with a peak photon density $max(h_{STED}) = 1.25 \times 10^{18}\,\mathrm{cm}^{-2}$. This was achieved by focusing 5.2 mW of average power through each objective. Further parameters are the same as for the measurement of

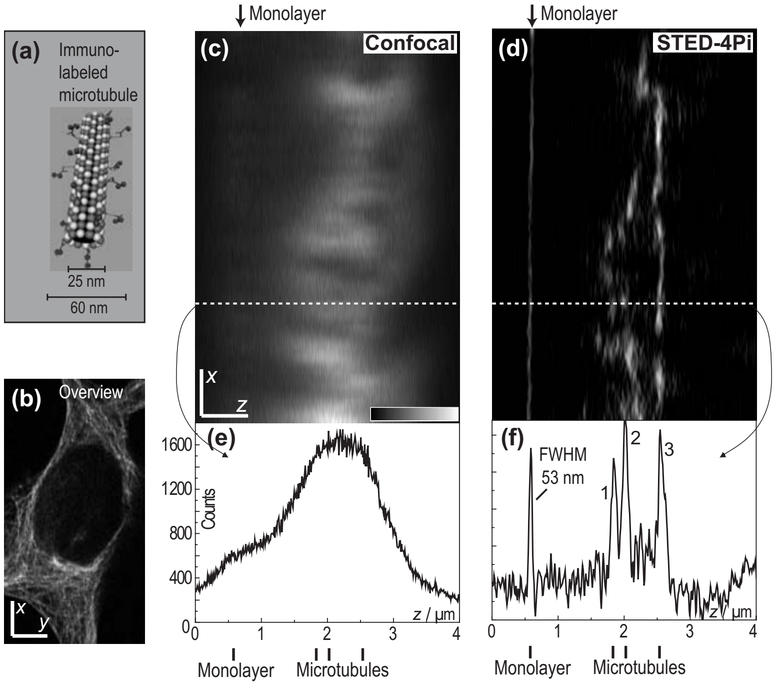

Figure 4.4: **Sub-diffraction imaging of immuno-labeled microtubules in human embryonic kidney cells,** marked with MR-121SE. (a) Sketch of typical dimensions of microtubule fluorescently decorated via a secondary antibody. (b) Overview image (xy) of the microtubular network in the cytoplasm. (c) and (d) Standard confocal and STED-4Pi xz-image recorded at the same site of the cell. In both images the pixel size was 95 nm x 9.8 nm in the x- and z-direction, respectively; the dwell time per pixel was 2 ms. (e,f) Corresponding profiles of the image data along the marked lines quantify the improved axial resolution of the STED-4Pi-microscopy mode. The peaks 1, 2, 3 of the microtubules are broader than the response to the monolayer.

$V(z)$ shown in Fig. 4.3(b). This z-response was used for a linear deconvolution of the xz-image in z-direction. The result is a sidelobe-free representation of the high resolution image.

The STED-4Pi image is significantly clearer. Whereas in the confocal image all of the adjacent microtubules appear as single blobs, in the STED-4Pi-counterpart most of them appear as distinct objects. The representation of a single tube is elongated along x, since the STED-4Pi does not affect the lateral resolution of ≈200 nm. Moreover, the sub-diffraction image shows that the brightness of the monolayer (left side of the images) is of the same order as that of the microtubules. In contrast, the larger focal spot of the confocal microscope integrates the fluorescence originating from several microtubules, thus giving an improper representation of the object brightness and fluorophore distribution in the image. The comparison of panel (c) with (d) underscores the importance of sub-diffraction resolution for quantitative microscopy at the nanoscale.

The mono-molecular layer beneath the cell gives a striking account of the image resolution within the cellular sample. In the raw data of the STED-4Pi image, the axial FWHM of the represented layer is 71.5±1.5 nm. This is slightly larger than the ≈50 nm in the deconvolved image (d). The 35% loss of resolution compared to the cell-free conditions of Fig. 4.3(b) is

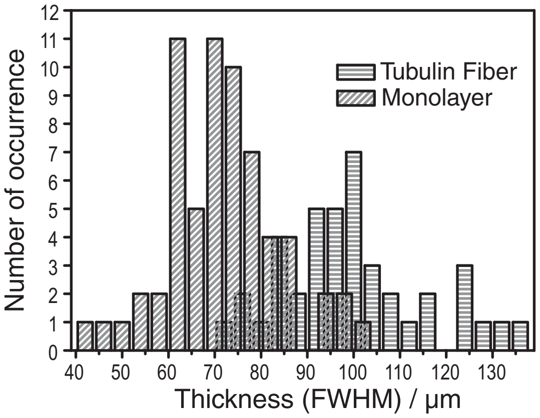

Figure 4.5: **Histogram of measured axial FWHM of the monolayer and the tubulin fibers.** The layer thickness was evaluated at different lines in the STED-4Pi images. For the tubulin data 10 images were analysed. Only smallest structures that could be attributed to single tubes with high probability were counted.

most likely caused by aberrations of the cell. The fact that in Fig. 4.4(d) the mono-layer appears as a straight line indicates that the interference of the counter-propagating depleting beams is not distorted by the cell. It also excludes the appearance of artifacts that eventually could be caused by sample induced phase changes of the interfering STED light.

Since it is known from electron microscopy [77], cytoplasmic microtubular labeled via a secondary antibody have a diameter of 60 nm. This is in the range of the resolution of the STED-4Pi microscope, as defined by the FWHM of h_{eff}. Indeed, a close look to image (d) in Fig. 4.4 reveals that the thickness of peaks or lines, which most likely can be attributed to single tubulin fibers, is larger than the representation of the mono-layer. The thickness of 50 structures that could be associated with high probability to single tubes, were analyzed from 10 images similar to Fig. 4.4(d). A histogram of the measured axial FWHM grouped in 4 nm broad channels is shown in Fig. 4.5. The FWHM were evaluated in the raw image, without any deconvolution processing. Evaluated thicknesses are presented for the mono-layer at different positions and for the 50 fibers representing peaks with different hatching of the bars. Analyzed by a Gaussian fit $A/(w\sqrt{\pi/2})\exp(-2(d-d_0)^2/w^2)$, the distribution is described by d_0=96 nm, w=24 nm for the tubulin fibers and by d_0=71 nm, w=20 nm for the mono-layer profiles. In a statistical meaning, the mono-layer is significantly thinner than the tubulin fibers. One has to take into account that the distribution of fiber diameters is spread by the fact that they are crossing the z axis under slightly varying angles, even if the main direction is perpendicular to z. However, 83% of the FWHM values were in the range of 86-127 nm, which is significantly larger than the 71 nm optical resolution derived from the mono-molecular layer. Even the smallest tubular peaks do not reach the mono-layer thickness d_0. As a simple approach, one can deduce the real object diameter from a quadratic subtraction of the FWHM of $V(z)$ from the measured FWHM of the tubular fibers. This leads to a estimated fiber diameter in the range of 60-70 nm which is in good agreement with the values obtained by electron microscopy [77]. So far, these are the first evidences that STED microscopy seems to be qualified to measure cellular structure dimensions at nanometer scale.

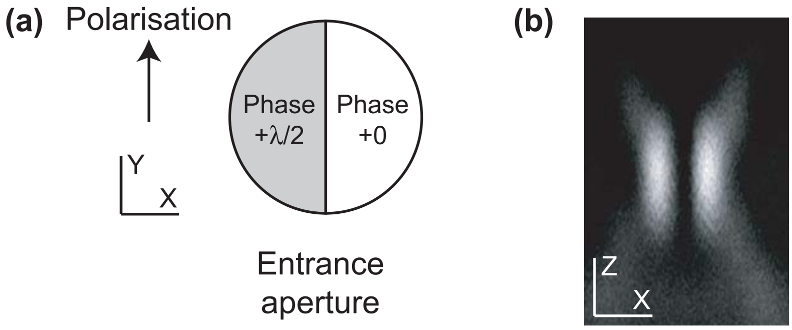

Figure 4.6: **STED-PSF for lateral resolution enhancement.** (a) shows the phase distribution in the entrance aperture of the objective lens. The polarisation direction must be chosen as in the sketch. (b) shows the focal distribution measured by reflection of a 80 nm gold micro-particle.

4.4 Lateral superresolution in immuno-fluorescence imaging of the microtubular network

The implementation of the further STED beam focused by only one objective with an annular phase filter now allows imaging of the microtubular network also with lateral resolution. The phase pattern produced with the spatial light modulator (see Fig. 4.1) and the corresponding PSF is shown in Fig. 4.6. The phase distribution of the STED light is chosen in a way, that the left part of the entrance pupil (with respect to the X-axis) is phase shifted by $\lambda/2$ [40]. Importantly, the polarization of the STED light must be set parallel to the separation line between the two phase areas (see Fig. 4.6(a)). Otherwise a significant amount of z-depolarized light is focused into the focal point. Thus the polarization of the STED beam as well as for the excitation beam is chosen to be parallel to the Y-axis. While a plane wave is focused constructively at the focal point, this phase distribution leads to destructive interference at the geometrical focus. However, two displaced and pronounced maxima appear along the X-axis, as shown in Fig. 4.6(b). This STED-PSF is well appropriate for increasing the X-resolution. With single molecules experiments, a resolution down to 28 nm could be proved with this technique [79], which is below the smallest structures expected in the microtubular network.

The sample preparation was done as described before, except that the cells were mounted in Mowiol[4], which made the samples much more stable for long-term storage (at 4°C). While the experiments in an aqueous environment proved that the STED method is applicable under live cell compatible conditions, the use of Mowiol samples makes the practical handling much easier. To match the refractive index of the immersion as good as possible, glycerol immersion objective lenses with NA 1.35 were utilized[5]. Therefore, the optical performance is not compromised. Furthermore, during the latest stage of the experiments, the 532 nm excitation source was replaced by a picosecond pulsed laser diode[6] that matches much better the excitation spectrum of MR-121 (see Fig. 4.2). The laser line was filtered in front of the

---

[4] Mowiol: 6 g Glycerol AR (Merck #4094), 2.4 g Mowiol 4-88 (Hoechst), 6 ml water, 12 ml 0.2 M Tris ph 8.5 buffer

[5] *PL APO 100x/1.35 Glycerol HCX CS* (Leica Microsystems AG, Wetzlar, Germany)

[6] *LDH-660* (PicoQuant Gmbh, Berlin, Germany)

fluorescence detector by a custom-made bandpass filter with steep edges[7].This improvement increased the detected fluorescence signal about 4-5 times compared to the 532 nm excitation and enabled faster scanning, meaning less photobleaching by the STED beam.

Lateral (XY) sections of the microtubular network of two exemplary cells are shown in Fig. 4.7. Images (a,c) show the STED images and (b,d) the subsequently recorded confocal counterparts. The acquisition time was 2.2 min for images (a,b) and and 4.4 min for images (c,d). The pixel dimension was 11×117 nm (images a,b) and 14.7×117 nm (images c,d). As expected, the images (a) and (c) appear sharper along the X-direction. The smallest structures have an FWHM of about 100-130 nm in X-direction and fibers at distances down to ≈110 nm are resolved, that cannot be separated in confocal mode (see profiles if Fig. 4.7(c)). In the confocal images, the diffraction limited resolution leads to a minimal FWHM of 220-240 nm of the represented fibers. The white arrows mark selected structures that become visible only in the STED images. For the depletion beam (λ_{STED}=785 nm) the photon density per pulse at the PSF-maxima was $max(h_{STED})$=5.7×10^{17} cm^{-2} in image (a) and 7.2×10^{17} cm^{-2}in image (c). This values were obtained by focusing an average power P_{STED} of 29.5 mW and 36.8 mW into the focus, respectively. After one scan, the fluorescence signal was reduced by≈22% by photobleaching of the STED light. Thus, in terms of photostability more STED power or further STED beams can be applied. The values of $max(h_{STED})$ are comparable to the values used in the STED-4Pi mode. However, the power P_{STED} needed to achieve a given photon density $max(h_{STED})$ is about 3 times higher than the necessary power focused through both objectives for the STED-4Pi-PSF. This is due to the fact that in the STED-4Pi case, the intensity maxima benefits from the constructive interference of the field amplitudes. Besides, the light is distributed into a larger area in the lateral STED-PSF.

To apply both the lateral and the axial STED-PSF simultaneously, the excitation light should be linearly polarized under 45 degrees to achieve acceptable depletion in both cases. The alternative way of circular polarizations for all beams cannot be chosen here because the annular phase filter of the single STED beam works only with linear polarized light. However, in both cases, P_{STED} must be increased by a factor of about two in order to retrieve the same STED efficiency[8]. Unfortunately, with the present laser, system such high powers are not available in connection with accurate spatial filtering of the expanded beam profiles, which is inevitable for the STED beams to produce unaberrated PSF with acceptable low intensity values of the central minimum. So far, a simultaneous action of both STED beams is hindered by technical limitations. It should be mentioned that this limitation is not conceptual. The experiments presented in this chapter demonstrate that, in principle, superresolution in both lateral and axial direction can be achieved at the same time. It can be expected that a 3D-resolution of at least 100×100×50 nm in immuno-fluorescence imaging will be realized in near future by further optimization of the laser system. This resolution will also be available in a live cell compatible environment. In connection with very photostable fluorescence dyes [79], simultaneous superresolution of about 20-30 nm in lateral and axial direction should be achievable by the presented techniques in far-field fluorescence microscopy.

---

[7] *HQ filter series* (Chroma Technology Corps, Rockingham, VT, USA)

[8] The precise conditions depend also on the molecular rotation between the excitation and the depletion.

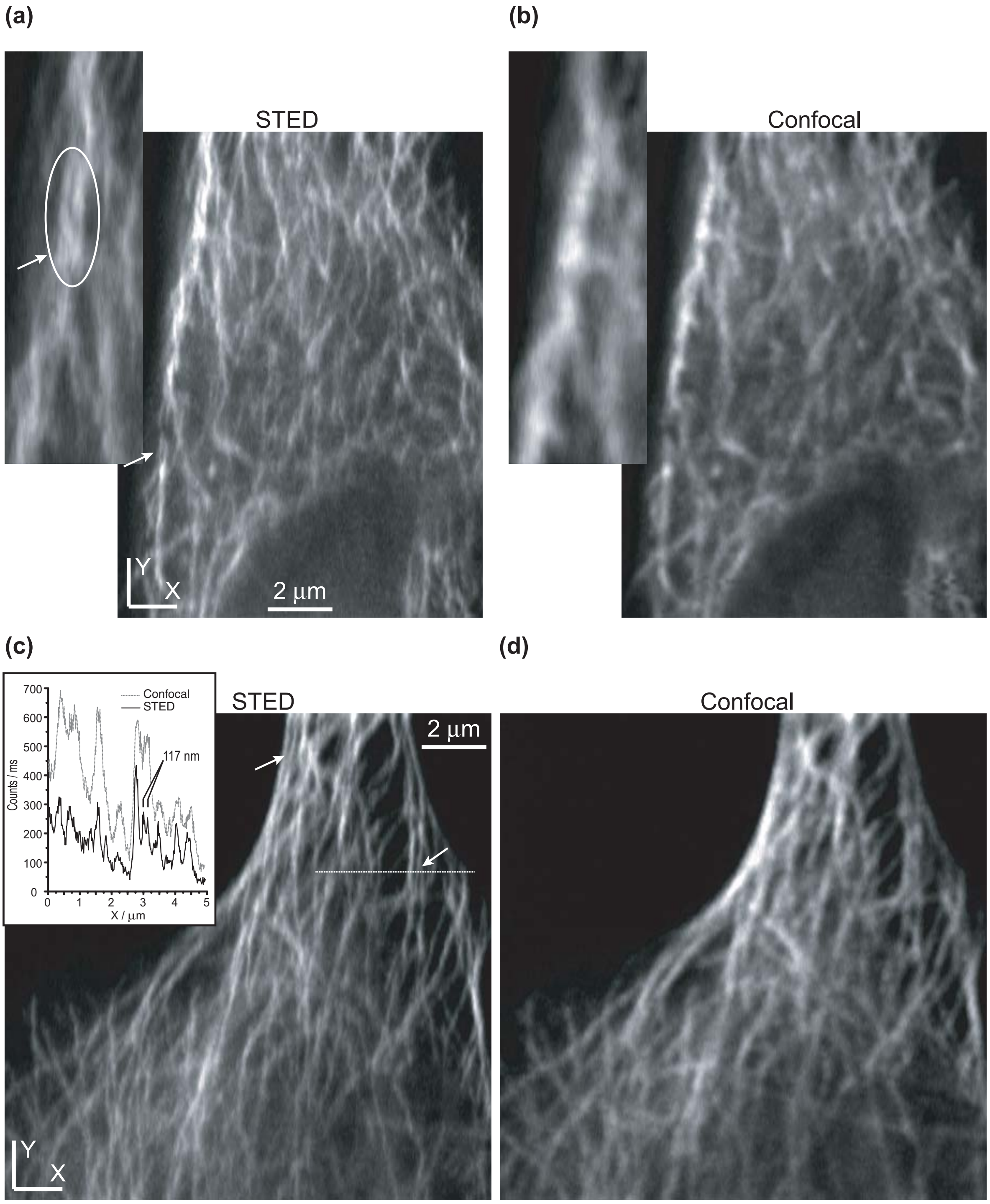

Figure 4.7: **Microtubular network of HEK cells with lateral superresolution in X-direction.** The images were obtained in the STED-4Pi microscope by use of an additional STED beam that is focused through only one of the objective lenses. This beam produces a focus with offset intensity maxima along the X-axis. (a,c) show the STED images, while (b,d) show the subsequently recorded confocal counterparts. The arrows and the insets in (a,b) point up structures that can only be resolved in the STED mode. The profiles in (c) quantify the resolution enhancement and the signal levels of the images. The STED profile shows fibers at a distance of only 117 nm.

Chapter 5

Conclusion

The implementation of STED in a 4Pi-confocal microscope was predicted to enforce the highest axial resolution yet achievable in optical far-field microscopy. Simulations within the scope of this thesis anticipated that resolutions of 30-40 nm should be possible under realistic experimental conditions. Indeed, ultimate resolution of 33 nm FWHM of the axial response could be demonstrated on layers of Pyridine 2. To the best of my knowledge, this is the highest resolving power ever achieved by focused light. The correspondent volume of exited molecules is 0.7 attoliter, defined by the FWHM values of the fluorescence signal.

This resolution range was also achieved inside cell samples. Images of RH414 labeled bacteria disclosed 40-50 nm resolution. Photostability studies with this exemplary bio-system showed that large pulse durations of >100 ps enable highly efficient STED and at the same time reduced photobleaching of the fluorophore. In consideration of this experience and by the first use of a STED-capable dye that can be used for immuno-labeling, immuno-fluorescence images of mammalian cells could be recorded with sub-diffraction resolution. Antibody labeled tubulin fibers of HEK cells were imaged at 50 nm axial resolution. Additionally, a further STED pulse was applied to the sample that provided superresolution of about 100 nm in the lateral direction. Even if the simultaneous application of lateral and axial superresolution still is under development, the results demonstrate that a real 3D-resolution of at least $100\times100\times50$ nm can be reached in optical imaging of biological samples. To date, these are not only the sharpest light microscopic images of the interior of cells, but are also a first evidence that optical 3D-imaging at the nanoscale becomes reachable. The adoption of a amino-reactive dye will now enable a wide field of cell-biological applications, which are accessible by antibody labeling.

Further progresses in the photostability of fluorescence dyes and their spectroscopic optimization might yield to a lateral and axial resolution of 20-30 nm[79]. Hence, focal volumes below 0.1 attoliter should be reachable. It should be emphasized that restrictions on the resolution power are given by the limited power of the STED-beams than can be applied under an acceptable amount of photodestructive effects. Also, imperfect central minima of the STED-PSF limit the maximal power of the STED beam.

For the purpose of high resolution imaging, the implementation of STED with shorter wavelengths should lead to an additional gain of about 30% in resolution, because of the reduced λ. Investigations of genetically coded fluorescent proteins (e.g. GFP, YFP, DsRED) under STED conditions should be a major goal. Together with immuno-techniques, this would enable STED for a majority of biological imaging applications and would be a further breakthrough in sub-diffraction imaging.

In principle, such results should be available as well with other saturation based techniques. An interesting approach is also novel types of switchable dyes or FRET pairs [35]. Their fluorescence property can be activated and deactivated by light-induced transitions, that should be saturable with low intensity cw lasers. These systems also have the potential to perform sub-diffraction imaging [27]. Fluorescence imaging at the nanometer range may also be possible by ground-state depletion or saturated pattern excitation if photostable conditions can be realized. While saturated excitation only involves one laser line for the absorption, there is a major difference compared to STED, GSD, or switchable dye systems. Only the latter techniques allow one to directly create a nanoscaled volume of molecules that are prepared in a certain spectroscopic state (i.e. in the exited state S_1), where the depleting beams prevent surrounding molecules from staying in that state. With other spectroscopic systems and adapted light interaction, this should not be restricted to the fluorescent sate S_1 of organic dye molecules, but also to other states, that are photodynamic or initial states of photochemical processes.[1] Therefore, STED and GSD should be able to control such processes at sub-diffraction sized dimensions. This could enable optical data storage at high densities, nano-lithography or the spatial control of photochemical steps on a broad basis [37, 8, 26]. Experimental investigations in this field should be performed in future. Also, it may have impact on FCS since the effective detection volume here is defined by the excited molecules as well. Sub-diffraction sized volumes will allow FCS at high concentrations, enabling chemical bindings with higher probability. This would bring FCS a big step forward towards monitoring chemical reactions [48].

---

[1] This could be a photoinduced proton transfer or cis-trans isomerization, for example.

Bibliography

[1] E. Abbe, *Beiträge zur theorie des mikroskops und der mikroskopischen wahrnehmung*, Arch. f. Mikroskop. Anat. **9** (1873), 413–420.

[2] D. Axelrrod and et al., *Total internal reflection fluorescence*, Topics in Fluorescence Spectroscopy: Biochemical Applications (J.R. Lakowicz, ed.), vol. 3, Plenum Press, New York, 1992.

[3] B. Bailey, D.L. Farkas, D.L. Taylor, and F. Lanni, *Enhancement of axial resolution in fluorescence microscopy by standing-wave excitation*, Nature **366** (1993), 44–48.

[4] G. Binnig, C.F. Quate, and Ch. Gerber, *Atomic force microscope*, Phys. Rev. Lett. **56** (1986), 930–933.

[5] G. Binnig and H. Rohrer, *Scanning tunneling microscopy*, Helvetica Physica Acta **55** (1982), 726–735.

[6] G. Binnig, H. Rohrer, Ch. Gerber, and E. Weibel, *Surface studies by scanning tunneling microscopy*, Phys. Rev. Lett. **49** (1982), 57–60.

[7] W. Denk, J.H. Strickler, and W. W. Webb, *Two-photon laser scanning fluorescence microscopy*, Science **248** (1990), 73–76.

[8] M. Dyba and S.W. Hell, *Focal spots of size l/23 open up far-field fluorescence microscopy at 33 nm axial resolution*, Phys. Rev. Lett. **88** (2002), 163901.

[9] M. Dyba and S.W. Hell, *Photostability of a fluorescent marker under pulsed excited-state depletion through stimulated emission*, Appl. Opt. **42** (2003), no. 25, 5123–5129.

[10] M. Dyba, S. Jakobs, and S.W. Hell, *Immunofluorescence stimulated emission depletion microscopy*, Nat. Biotechnol. **21** (2003), no. 11, 1303–1304.

[11] M. Dyba, T. A. Klar, S. Jakobs, and S. W. Hell, *Ultrafast dynamics microscopy*, Appl. Phys. Lett. **77** (2000), 597–599.

[12] A. Einstein, *Zur quantentheorie der strahlung*, Physik. Zeitschr. **18** (1917), 121–128.

[13] P. Fromherz and C.O. Müller, *Voltage-sensitive fluorescence of amphiphilic hemicyanine dyes in neuron membrane*, Biochim. Biophys. Acta **1150** (1993), no. 2, 111–122.

[14] M. Göppert-Mayer, *Über elementarakte mit zwei quantensprüngen*, Ann. Phys. Lpzg **9** (1931), 273–295.

[15] A. Grinvald, B.M. Salzberg, V. Lev-Ram, and R. Hildesheim, *Optical recording of synaptic potentials from processes of single neurons using intracellular potentiometric dyes*, Biophys. J. **51** (1987), 643–651.

[16] I. Gryczynski, J. Kusba, Z. Gryczynski, H. Malak, and J.R. Lakowicz, *Anisotropy spectra of the solvent-sensitive fluorophore 4-dimethylamino-4'-cyanostilbene in the presence of light quenching*, J. Fluoresc. **8** (1998), no. 3, 253–261.

[17] M. Gu, *Principles of three-dimensional imaging in confocal microscopes*, World Scientific, Singapore, 1996, p. 142.

[18] M. G. Gustafsson, D. A. Agard, and J. W. Sedat, *3d widefield microscopy with two objective lenses: experimental verification of improved axial resolution*, Three-Dimensional Microscopy: Image Acquisition and Processing III (C. Cogswell, G.S. Kino, and T. Wilson, eds.), 1996.

[19] M. G. L. Gustafsson, *Surpassing the lateral resolution limit by a factor of two using structured illumination microscopy*, J. Microsc. **198** (2000), no. 2, 82–87.

[20] M. G. L. Gustafsson, D. A. Agard, and J. W. Sedat, *Sevenfold improvement of axial resolution in 3d widefield microscopy using two objective lenses*, Proc. SPIE **2412** (1995), 147–156.

[21] B. Hecht, H. Bielefledt, Y. Inouyne, D.W. Pohl, and L. Novotny, *Facts and artifacts in near-field optical microscopy*, J. of Appl. Phys. **81** (1997), 1492–2498.

[22] R. Heintzmann, T. M. Jovin, and C. Cremer, *Saturated patterned excitation microscopy-a concept for optical resolution improvement*, J. Opt. Soc. Am. A **19** (2002), 1599–1609.

[23] S. Hell and E. H. K. Stelzer, *Properties of a 4pi-confocal fluorescence microscope*, J. Opt. Soc. Am. A **9** (1992), 2159–2166.

[24] S. W. Hell, *Increasing the resolution of far-field fluorescence light microscopy by point-spread-function engineering*, Topics in Fluorescence Spectroscopy (J.R. Lakowicz, ed.), vol. 5, Plenum Press, New York, 1997, pp. 361–422.

[25] S. W. Hell and E. H. K. Stelzer, *Fundamental improvement of resolution with a 4pi-confocal fluorescence microscope using two-photon excitation*, Opt. Commun. **93** (1992), 277–282.

[26] S.W. Hell and M. Dyba, *Method and device for physically defined excitation of an optical transition*, 15. 05. 2003, European Patent EP 200210456.

[27] S.W. Hell, S. Jakobs, and L. Kastrup, *Imaging and writing at the nanoscale with focused visible light through saturable optical transitions*, Appl. Phys. A **77** (2003), 859–860.

[28] S.W. Hell and M. Kroug, *Ground-state depletion fluorescence microscopy, a concept for breaking the diffraction resolution limit*, Appl. Phys. B **60** (1995), 495–497.

[29] S.W. Hell, A. Utz, P.E. Hänninen, and E. Soini, *Pulsed laser fluorophore deposition: a method for measuring the axial resolution in two-photon fluorescence microscopy*, J. Opt. Soc. Am. A **12** (1995), no. 9, 2072–2076.

[30] S.W. Hell and J. Wichmann, *Breaking the diffraction resolution limit by stimulated emission: stimulated emission depletion microscopy*, Opt. Lett. **19** (1994), no. 11, 780–782.

[31] P. Hänninen, *Beyond the diffraction limit*, Nature **419** (2002), 802.

[32] P. E. Hänninen, M. Schrader, E. Soini, and S. W. Hell, *Two-photon excitation fluorescence microscopy using a semiconductor laser*, Bioimaging **3** (1995), 70–75.

[33] R. Hooke, *Micrographia*, first ed., London, 1665.

[34] A. Hopt and E. Neher, *Highly nonlinear photodamage in two-photon fluorescence microscopy*, Biophys. J. (2001), 2029–2036.

[35] M. Irie, T. Fukaminato, T. Sasaki, N. Tamai, and T. Kawai, *A digital fluorescent molecular photoswitch*, Nature **420** (2002), 759–760.

[36] M. Kasha, *Paths of molecular excitation*, Rad. Res. Suppl. 2 (1960), no. 243-275.

[37] T. A. Klar, *Progress in stimulated emission depletion microscopy*, Doctoral thesis, Rupertus Carola University of Heidelberg, 2001.

[38] T. A. Klar, S. Jakobs, M. Dyba, A. Egner, and S. W. Hell, *Fluorescence microscopy with diffraction resolution limit broken by stimulated emission*, Proc. Natl. Acad. Sci. USA **97** (2000), 8206–8210.

[39] T.A. Klar, M. Dyba, and S.W. Hell, *Stimulated emission depletion microscopy with an offset depleting beam*, Appl. Phys. Lett. **78** (2001), no. 4, 393–395.

[40] T.A. Klar, E. Engel, and S.W. Hell, *Breaking abbe's diffraction resolution limit in fluorescence microscopy with stimulated emission depletion beams of various shapes*, Phys. Rev. E **64** (2001), 066613, 1–9.

[41] T.A. Klar and S.W. Hell, *Subdiffraction resolution in far-field fluorescence microscopy*, Opt. Lett. **24** (1999), no. 14, 954–956.

[42] K. König, T. W. Becker, P. Fischer, I. Riemann, and K-J Halbhuber, *Pulse-length dependence of cellular response to intense near-infrared laser pulses in multiphoton microscopes*, Opt. Lett. **24** (1999), no. 2, 113–115.

[43] H.J. Koester, D. Baur, R. Uhl, and S.W. Hell, *Ca (2+*exp) fluorescence imaging with pico- and femtosecond two-photon excitation: Signal and photodamage*, Biophys. J. **77** (1999), 2226–2236.

[44] R.V. Krishnan, R. Varma, and S. Mayor, *Fluorescence methods to probe nanometer-scale organization of molecules in living cell membranes*, J. Fluoresc. **11** (2001), no. 3, 211–213.

[45] J. R. Lakowicz, *Principles of fluorescence spectroscopy*, Plenum Press, New York, 1983.

[46] J.R. Lakowicz, I. Gryczynski, J. Kusba, and V. Bogdanov, *Light quenching of fluorescence: A new method to control the excited state lifetime and orientation of fluorophores*, Photochem. and Photobiol. **6** (1994), 546–562.

[47] F. Lanni, *Applications of fluorescence in the biomedical sciences*, 1 ed., Liss, New York, 1986.

[48] T.A. Laurence and S. Weiss, *How to detect weak pairs*, Science **299** (2003), no. 5607, 667–668.

[49] A. Lewis, M. Isaacson, A. Harootunian, and A. Murray, *Development of a 500 a resolution light microscope*, Ultramicroscopy **13** (1984), 227–231.

[50] J. Lippincott-Schwartz, E. Snapp, and A Kenworthy, *Studying protein dynamics in living cells*, Nature Reviews **2** (2001), 444–456.

[51] M. V. Matz, A. F. Fradkov, Y. A. Labas, A. P. Savitsky, A. G. Zaraisky, M. L. Markelov, and S. A. Lukyanov, *Fluorescent proteins from nonbioluminescent anthozoa species*, Nature Biotech. **17** (1999), no. 10, 969–973.

[52] W. Meyer-Ilse, D. Hamamoto, A. Nair, S.A. Lelievre, G. Denbeaux, L. Johnson, A.L. Pearson, D. Yager, M.A. Legros, and C.A. Larabell, *High resolution protein localization using soft x-ray microscopy*, J. Microsc. **201** (2000), no. 3, 395–403.

[53] J. Michaelis, C. Hettich, J. Mlynek, and V. Sandoghdar, *Optical microscopy using a single-molecule light source*, Nature **405** (2000), no. 18. May, 325–327.

[54] M. Minsky, *Microscopy apparatus*, 1961.

[55] L. Moreaux, O. Sandre, S. Charpak, M. Blanchard-Desce, and J. Mertz, *Coherent scattering in multi-harmonic light microscopy*, Biophys. J. **80** (2001), 1568–1574.

[56] M. Nagorni and S. W. Hell, *Coherent use of opposing lenses for axial resolution increase in fluorescence microscopy. i. comparative study of concepts*, J. Opt. Soc. Am. A **18** (2001), no. 1, 36–48.

[57] S.K. Parida and B.K. Mishra, *Adsorption of styryl pyridinium dyes on silica gel*, J. of Colloid and Interface Sci. **182** (1996), 473–477.

[58] ______, *Adsorption of styryl pyridinium dyes on alkali treated silica*, Indian J. of Chem. **37A** (1998), 618–625.

[59] G. H. Patterson and D. W. Piston, *Photobleaching in two-photon excitation microscopy*, Biophys. J. **78** (2000), 2159–2162.

[60] J. Pawley, *Handbook of biological confocal microscopy*, Plenum Press, New York, 1995.

[61] D.W. Pohl, W. Denk, and M. Lanz, *Optical stethoscopy: Image recording with resolution l/20*, Appl. Phys. Lett. **44** (1984), 651–653.

[62] B.A. Pollok and R. Heim, *Using gfp in fret-based applications*, Trends Cell Biol. **9** (1999), no. 2, 57–60.

[63] W. H. Press, B. P. Flannery, S. A. Teukolsky, and W. T. Vetterling, *Numerical recipes in c*, 2 ed., Cambridge University Press, 1993.

[64] Lord Rayleigh, *On the theory of optical images, with special reference to the microscope*, Philosophical Magazine **XLII** (1896), 167–195.

[65] L. Reimer, *Scanning electron microscopy*, Springer Series in Optical Sciences, Springer-Verlag, Berlin, Heidelberg, New York, Tokyo, 1985.

[66] B. Richards and E. Wolf, *Electromagnetic diffraction in optical systems ii. structure of the image field in an aplanatic system*, Proc. R. Soc. Lond. A **253** (1959), 358–379.

[67] E.J. Sanchez, L. Novotny, and X.S. Xie, *Near-field fluorescence microscopy based on two-photon excitation with metal tips*, Phys. Rev. Lett. **82** (1999), 4014–4017.

[68] F. P. Schäfer, *Dye lasers*, Springer, Berlin, Heidelberg, 1973.

[69] D.J. Stephens and V.J. Allen, *Light microscopy techniques for live cell imaging*, Science **300** (2003), 82–91.

[70] J.A Steyer and W. Almers, *A real-time view of life within 100 nm of the plasma membrane*, Nat. Rev. Mol. Cell Biol. **2** (2001), 268–275.

[71] E.H. Synge, *A suggested method for extending microscopic resolution into the ultra-microscopic region*, Philos. Mag. **6** (1928), 356.

[72] A.N. Tikhonov and V.Y. Arsenin, *Solutions of ill-posed problems*, Wiley, New York, 1977.

[73] P. Tinnefeld, V. Buschmann, D. P. Herten, K. T. Han, and M. Sauer, *Confocal fluorescence lifetime imaging microscopy (flim) at the single molecule level*, Single Mol. **1** (2000), 215–223.

[74] D. Toomre and D.J. Manstein, *Lighting up the cell surface with evanescent wave microscopy*, Trends in Cell Biol. **11** (2001), no. 7, 298–303.

[75] G. Toraldo di Francia, *Supergain antennas and optical resolving power*, Nuovo Cimento Suppl. **9** (1952), 426–435.

[76] R.Y. Tsien, *The green fluorescent protein*, Annu. Rev. Biochem. **67** (1998), 509–544.

[77] K. Weber, P. C. Rathke, and M. Osborn, *Cytoplasmic microtubular images in glutaraldehyde-fixed tissue culture cells by electron microscopy and by immunofluorescence microscopy*, Proc. Natl. Acad. Sci. USA **75** (1978), no. 4, 1820.

[78] V. Westphal, C. M. Blanca, M. Dyba, L. Kastrup, and S. W. Hell, *Laser-diode-stimulated emission depletion microscopy*, Appl. Phys. Lett. **82** (2003), no. 18, 3125–3127.

[79] V. Westphal, L. Kastrup, and S. W. Hell, *Lateral resolution of 28nm (lambda/25) in far-field fluorescence microscopy*, Appl. Phys. B **77** (2003), no. 4, 377–380.

[80] T. Wilson, *Confocal microscopy*, Academic Press, London, 1990.

[81] T. Wilson and C.J.R. Sheppard, *Theory and practice of scanning optical microscopy*, Academic Press, New York, 1984.

[82] F. Zenhausern, M.P O‘Boyle, and H.K. Wickramasinghe, *Apertureless near-field optical microscope*, Appl. Phys. Lett. **65** (1994), 1623–1625.

Appendix

RH414 staining of *bacillus megaterium*

The bacteria (wild type strain DSM 90) were grown in standard nutrient solution into log-phase. After centrifugation (1 min, 3400 rpm) they were suspended in a phosphate buffer solution[2]. Afterwards, the dye RH414[3] was added (10 μM). The bacteria were washed after 30-60 min by a centrifugation step and immersed in PBS. They were mounted onto a cover slip, whose surface was previously covered with poly-L-lysine[4] (1 drop for 5 min). Non-adhering bacteria were washed away and fresh nutrient solution was applied as mounting medium (refractive index n=1.34 at room temperature).

MR-121 labeling of silan-treated coverslips surfaces

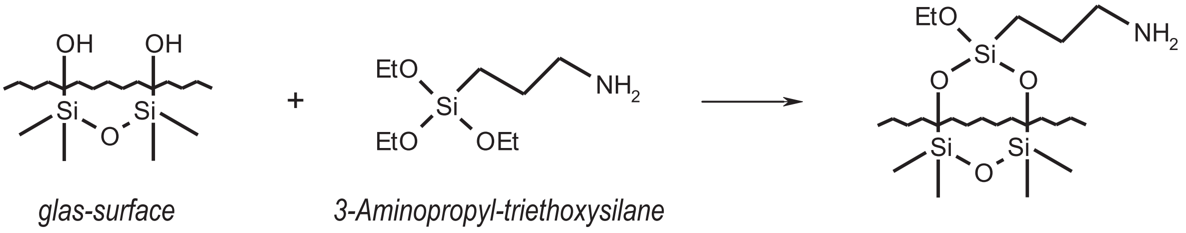

Figure 5.1: Silanisation of silica surfaces (glass). The glass surface is treated with NaOH to produce a large number of OH-groups. 3-aminopropyl-triethoxysilan binds covalently to the OH-groups. At the NH_2 site, amino reactive dyes as MR-121SE can bind and build a mono-molecular layer.

The functionalized dye MR-121SE can be used according to standard procedures to prepare a coverslip surface with a stable, monomolecular layer. First, the coverslip needs to be treated with silane, as shown in Figure 5.1:

- Coverslips were washed with 3% Mucasol[5] for 10 min in ultrasound.
- Coverslips were treated with 1M NaOH for 15 min in ultrasound.

---

[2] *PBS:* 137 mM $NaCl$, 2.7 mM KCl, 4.3 mM Na_2HPO_4, 1.4 mM KH_2PO_4, pH=7.3

[3] *N-(3-triethylammoniumpropyl)-4-{4-[4-(diethylamino)phenyl]butadienyl} pyridinium dibromide* (Molecular Probes Inc., Eugene, OR, USA)

[4] *Poly-*L*-lysine solution* (*#P 8920*; Sigma Dioagnostics Inc., St. Louis, MO, USA)

[5] *Mucasol #60434* (Brand GmbH, Wertheim/Main, Germany)

- After a washing step in purified water and complete drying, the coverslips were placed in 90ml Dimethyl sulfoxide + 5 ml (3-Aminopropyl)-triethoxysilane[6]. Under slow agitation, the solution is heatedh to 100°C for≈6.
- Coverslips were removed and thoroughly washed with purified water.
- Silane-treated coverslip can be stored at 4°C (at least some weeks to months).

A drop of MR-121SE dissolved in dimethyl-sulfoxide (about 10-100 μM) is placed for 10-30 min on the glas surface and is finally washed away with purified water. (Use only very freshly prepared solutions, since the functional group is not stable in solution.) The prepared coverslips can be stored dark at 4°C for at least a couple of weeks and can be used for online adjustment of the STED-4Pi microscope in conjunction with any arbitrary sample.

Immuno-fluorescence staining of HEK cells

Human embryonic kidney (HEK) cells[7], grown on a coverslip, were fixed with cold methanol and their microtubuli labeled with a mouse anti-β-tubulin monoclonal antibody[8]. For the secondary antibody, the dye was coupled via its succinimidyl ester group to an anti-mouse IgG[9]. The cells were mounted between two coverslips that were manually selected according to their thickness. For the water immersion objectives a pH-buffer solution (PBS) with a refractive index almost matching that of water was used. For the glycerol objectives Mowiol antifade medium was used[10]. This ensures spectroscopic conditions as needed for live cell imaging and is therefore a good test for future *in-vivo* STED microscopy.

---

[6] *(3-Aminopropyl)-triethoxysilane #09324* (Sigma-Aldrich Chemie GmbH, Tuafkirchen, Germany)

[7] *ER-293* (#222110 Stratagene Europe, Amsterdam, Netherlands)

[8] Boehringer, Mannheim, Germany

[9] Jackson ImmunoResearch Laboratories, West Grove, USA

[10] *Mowiol:* 6 g Glycerol AR (#4094, Merck, Darmstadt, Germany), 2.4 g Mowiol 4-88 (Hoechst, Germany), 6 ml water, 12 ml 0.2 M Tris ph 8.5 buffer

Acknowledgements

I would like to express grateful thank to all people who contributed their help and supported to the success of this work.

At first I want to thank Priv. Doz. Dr. Stefan Hell not only for proposing me this fascinating field of modern optical microscopy as the topic of my work, but also for his continuous support by his outstanding and long lasting experience. In difficult situations he contributed often with valuable discussions and facilitated excellent experimental conditions.

I also would like to thank Prof. Josef Bille at the University of Heidelberg for his interest in my work and for being the second referee of my thesis.

My special thanks go to Katrin Willig, who often contributed valuable discussions about the STED project and made the everyday labwork much more likeable. Thank you also for encouraging me during the less successful periods of my work!

Many thanks to Dr. Stefan Jakobs, Sylvia Löbermann for their support with bacteria and HEK cells and for preparing biological samples.

Furthermore, I would like to thank many other members of our department. Thanks to Dr. Andreas Schönle for helpful discussions and the development and support of the comfortable setup-control and data analysis software “Imspector”, which is more often used than appreciated. Also many thanks for valuable discussions to Lars Kastrup, Dr. Christian Eggeling, Dr. Volker Westphal, Dr. Johann Engelhardt and Jan Keller who also worked on different aspects of the STED project.

I also want to acknowledge the continuous technical support by Harald Meyer, Jaydev Jethwa, Donald Ouw and Rainer Pick, who often helped me in electronical, optical or chemical questions.

I grateful like to acknowledge the work of our precision mechanic group, especially to Dieter-Jürgen Czudnochowski, and of our precision optics group under direction of Wolfgang Sauermann and Wolfgang Kluge. They all supported the development of the STED-4Pi microscope with their competent aid.

Thanks to Lars Kastrup, Katrin Willig and Jaydev Jethwa for reading the manuscript.

Finally, I wholeheartedly want to say “Thank you” to my parents, who supported me not only materially from the very beginning up to now. Thanks to them and my family, that I always can rely on you!

Publications resulting from this thesis

[1] M. Dyba and S.W. Hell, *Focal spots of size $\lambda/23$ open up far-field fluorescence microscopy at 33 nm axial resolution*, Phys. Rev. Lett. **88** (2002), 163901.

[2] M. Dyba and S.W. Hell, *Photostability of a fluorescent marker under pulsed excited-state depletion through stimulated emission*, Appl. Opt. **42** (2003), no. 25, 5123-5129.

[3] M. Dyba, S. Jakobs, and S.W. Hell, *Immunofluorescence stimulated emission depletion microscopy*, Nature Biotechnol. **21** (2003), no. 11, 1303-1304.

[4] S.W. Hell and M. Dyba, *Method and device for physically defined excitation of an optical transition*, 15. 05. 2003, European Patent EP 200210456.